

Clearance of defective muscle stem cells by senolytics restores myogenesis in myotonic dystrophy type 1

Received: 24 June 2022

Accepted: 22 June 2023

Published online: 19 July 2023

 Check for updates

Talita C. Conte^{1,2}, Gilberto Duran-Bishop^{1,3}, Zakaria Orfi^{1,2}, Inès Mokhtari^{1,4,5}, Alyson Deprez^{1,2}, Isabelle Côté⁵, Thomas Molina^{1,2}, Tae-Yeon Kim^{1,6}, Lydia Tellier^{1,7}, Marie-Pier Roussel^{5,8}, Damien Maggiorani^{1,2}, Basma Benabdallah¹, Severine Leclerc¹, Lara Feulner¹, Ornella Pellerito¹, Jean Mathieu^{5,9}, Gregor Andelfinger^{1,10}, Cynthia Gagnon^{5,9}, Christian Beauséjour^{1,2}, Serge McGraw^{1,3}, Elise Duchesne^{4,5,11}✉ & Nicolas A. Dumont^{1,7,11}✉

Muscle stem cells, the engine of muscle repair, are affected in myotonic dystrophy type 1 (DM1); however, the underlying molecular mechanism and the impact on the disease severity are still elusive. Here, we show using patients' samples that muscle stem cells/myoblasts exhibit signs of cellular senescence in vitro and in situ. Single cell RNAseq uncovers a subset of senescent myoblasts expressing high levels of genes related to the senescence-associated secretory phenotype (SASP). We show that the levels of interleukin-6, a prominent SASP cytokine, in the serum of DM1 patients correlate with muscle weakness and functional capacity limitations. Drug screening revealed that the senolytic BCL-XL inhibitor (A1155463) can specifically remove senescent DM1 myoblasts by inducing their apoptosis. Clearance of senescent cells reduced the expression of SASP, which rescued the proliferation and differentiation capacity of DM1 myoblasts in vitro and enhanced their engraftment following transplantation in vivo. Altogether, this study identifies the pathogenic mechanism associated with muscle stem cell defects in DM1 and opens a therapeutic avenue that targets these defective cells to restore myogenesis.

Myotonic dystrophy type 1 (DM1) is a rare disease that affects approximately 1:8,000 individuals in the world^{1,2}. DM1 is caused by an unstable (CTG) nucleotide repeat in the *dystrophia myotonica protein kinase (DMPK) gene*³. CTG repeats in DNA lead to toxic mRNA accumulation causing splicing defects mainly attributable to binding

protein sequestration. In healthy individuals, the *DMPK* alleles have 5 to 37 CTG repeats, but in DM1, there can be hundreds to thousands of these repeats; with the number of repeats partially correlating with the age of onset and the severity of the disease⁴⁻⁷. Patients are classified into five clinical phenotypes according to the CTG expansion size, and

¹CHU Sainte-Justine Research Center, Montreal, QC, Canada. ²Department of pharmacology and physiology, Faculty of Medicine, Université de Montréal, Montreal, QC, Canada. ³Department of obstetrics and gynecology, Faculty of Medicine, Université de Montréal, Montreal, QC, Canada. ⁴Department of Health Sciences, Université du Québec à Chicoutimi, Saguenay, QC, Canada. ⁵Neuromuscular diseases interdisciplinary research group (GRIMN), Saguenay-Lac-St-Jean Integrated University Health and Social Services Center, Saguenay, QC, Canada. ⁶Department of microbiology, infectiology and immunology, Faculty of Medicine, Université de Montréal, Montreal, QC, Canada. ⁷School of rehabilitation, Faculty of Medicine, Université de Montréal, Montreal, QC, Canada. ⁸Department of Fundamental Sciences, Université du Québec à Chicoutimi, Saguenay, QC, Canada. ⁹CHU Sherbrooke Research Center, and Faculty of Medicine and Health Sciences, Université de Sherbrooke, Sherbrooke, QC, Canada. ¹⁰Department of Pediatrics, Faculty of Medicine, Université de Montréal, Montreal, QC, Canada. ¹¹These authors contributed equally: Elise Duchesne, Nicolas A. Dumont. ✉e-mail: elise1_duchesne@uqac.ca; nicolas.dumont.1@umontreal.ca

the occurrence and onset of their main symptoms: congenital, infantile, juvenile, adult, and late-onset⁸.

DMI is a multisystemic disease that affects different organs, and particularly the skeletal muscles, leading to progressive weakness and atrophy⁹. Muscle stem cells (MuSCs), which contribute to skeletal muscle growth and repair are also affected in this disease⁵. In healthy condition, quiescent MuSCs are activated after an injury and become myoblasts that proliferate extensively before exiting the cell cycle to self-renew or to differentiate and fuse to form new myofibers¹⁰. Previous studies performed on mixed cell populations (non-purified by FACS) extracted from skeletal muscle samples of DMI patients showed that these cells exhibit signs of cellular senescence (a state of irreversible cell cycle arrest), such as enzymatic senescence-associated β -Galactosidase (SA- β -Gal) activity, expression of the cell cycle inhibitor p16, loss of nuclear integrity, and nuclear envelope invagination^{11,12}. It was shown using in vitro models of DMI that cellular senescence is independent from telomere shortening but is rather induced by the activity of the cell cycle inhibitor p16 and/or p21 in response to CTG-related stress^{12–14}. This increase in cellular senescence is associated with reduced proliferative capacity of DMI myoblasts and delayed differentiation and fusion into myofibers^{5,12,14}. Overexpression of cyclin-dependent kinase 4 (Cdk4) to bypass p16-induced senescence restored the proliferation of DMI cells to the level of healthy control cells¹².

In addition to decreasing the pool of competent cells, senescent cells secrete a broad range of molecules including proinflammatory cytokines (e.g., IL-1, IL-6) and matrix proteinases (e.g., MMP1, MMP3). This cocktail, known as the Senescence-Associated Secretory Phenotype (SASP), alters the microenvironment and leads to detrimental changes in neighboring cells and in the whole organism^{15,16}. Particularly, IL-6 is associated with muscle wasting conditions and promotes the exhaustion of the MuSC pool^{17–19}. Chronic exposure to SASP is considered as one of the major sources of deleterious effects on tissue maintenance and regenerative capacity^{15,20}; however, its impact on DMI pathogenesis has not been investigated yet.

Considering that senescent cells accumulate with time and have detrimental impacts on neighboring cells, they represent an attractive target for the treatment of many disorders²¹. Pioneer studies showed that genetic removal of senescent cells expressing the cell cycle inhibitor p16 in aging mice enhances their lifespan^{20,22}. Moreover, pharmacological compounds, called senolytics, can selectively eliminate senescent cells²³, which reduces the production of frailty-related proinflammatory cytokines in aged mice, and improves physical function and lifespan²⁴. We hypothesized that senolytics hold great therapeutic potential for the treatment of DMI considering that this disease has been described as a progeroid syndrome (i.e. mimicking premature aging)^{11,25}, and that skeletal muscles in DMI share many similarities with aged muscles such as cellular senescence, MuSC defects, and muscle wasting²⁶. However, the impact of senolytics in muscular diseases such as DMI has never been investigated.

Here, we generated a single-cell transcriptomic atlas of DMI samples to identify the molecular signature of myogenic cell subpopulations. Using myoblasts isolated from DMI patients and age- and sex-matched healthy controls, we identified a specific subset of senescent-like cells expressing high levels of SASP. We confirmed cellular senescence using different markers (p16, p21, SA- β -Gal) in primary myoblasts of DMI patients in vitro and in skeletal muscle biopsies in situ. Furthermore, we demonstrated that the level of IL-6, a key SASP cytokine, is correlated with upper- and lower-limb muscle weakness as well as functional capacity limitations in individuals affected by DMI. Thereafter, we screened different senolytic drugs and have identified the B-cell lymphoma-extra large (BCL-XL) inhibitor, A1155463, as the most promising molecule to eliminate specifically senescent myoblasts cultured from DMI patients' samples, without affecting cells cultured from healthy controls' samples. Clearance of senescent cells reduced the expression of harmful SASP, which restored the myogenesis potential of the

myoblasts in vitro and following cell transplantation in vivo. Altogether, these findings support the importance of cellular senescence in the disease severity, and the therapeutic potential of senolytics to target defective myogenic cells and reduce SASP expression in DMI.

Results

Single-Cell RNAseq identifies a subset of senescent cells in DMI myoblasts

Considering that cellular senescence only affects a subset of cells at a given moment, we took advantage of the single-cell RNA sequencing (scRNAseq) technology to identify the distinct transcriptional profile in cellular subpopulations of DMI myoblasts. Myoblasts were sorted by FACS (Supplementary Fig. 1a) and purity was confirmed by immunofluorescence (Supplementary Fig. 1b, c). Single-cell transcriptomic sequencing was performed on pooled myoblasts at the same early passage (P4) from 3 DMI patients (juvenile phenotype) and 3 age- and sex-matched healthy controls (Supplementary Table 1). After filtering and removal of doublets in the sequencing data, we analyzed 1,613 control cells and 1,714 DMI patient cells (Supplementary Fig. 2a–d). Both controls and DMI cells express high levels of myogenic cell markers such as *CD82*, *ITGB1* (*CD29*), *MYF5*, *MYOD1*, *NCAMI* (*CDS6*), and *DES*, as well as low levels of the fibroadipogenic (*PDGFRa* and *CD34*), endothelial (*CD31* and *TIE1*), and myeloid (*CD11B* and *CD45*) cell markers (Supplementary Fig. 2e). UMAP plot of merged control and patient cells revealed that these cells cluster differently (Fig. 1a). Differential expression analysis showed that the expression of 516 genes was significantly changed ($p < 10e-6$; $n = 266$ downregulated and $n = 250$ upregulated) in DMI patients compared to controls (Fig. 1b and Supplementary Data 1). Compared to healthy control cells, DMI cells showed lower expression in genes associated to myogenic markers (e.g., *MYF5*, *MYOD1*, *MYF6*, *SIX1*), extracellular matrix components (e.g., *COL1A1*, *COL1A2*, *COL3A1*, *COL5A2*, *LAMA2*, *FNI*), Notch signaling (e.g., *HEYL*, *RBPJ*), and cell cycle (e.g., *CENPF*, *CCNA2*, *CCNB1*, *CCNB2*, *CDK1*, *MKI67*) (Fig. 1b, c and Supplementary Data 1). Downregulated genes in DMI cells were associated to biological processes related to cell cycle, muscle structure development, and extracellular matrix organization (Fig. 1d, f). Top upregulated genes in DMI cells included cytokines/chemokines related to inflammation (e.g., *CXCL1*, *CXCL2*, *CXCL3*, *CXCL5*, *CXCL6*, *CXCL8*, *IL1B*, *IL6*, *CSF3*), and metalloproteinases (e.g., *MMP1*, *MMP3*) (Fig. 1b, c and Supplementary Data 1). Upregulated genes in DMI cells were enriched for biological functions including cytokine signaling, cellular response to stress, reactive oxygen species (ROS) production, autophagy, apoptosis, and senescence (Fig. 1e, g).

SCENIC analysis was used to predict transcription factors regulating the gene sets. Results showed that downregulated genes are controlled by different transcription factors related to myogenesis (e.g., *MYF5*, *MYOD1*, *MYF6*, *SIX1*), while for the genes upregulated in DMI the transcription factors related to the NF- κ B pathway (e.g., *NFKB1*, *NFKB2*, *REL*, *RELB*) were identified (Fig. 1h, i). STRING analysis performed on the top SASP factors and the top transcription factors upregulated in DMI, revealed strong interaction with the anti-apoptotic BCL pathway that is a key player in the regulation of cellular senescence (Fig. 1j).

UMAP plot showed that cells expressing high levels of pro-inflammatory cytokines (e.g., *CXCL1*, *CXCL8*, *IL1B*, *IL6*) in DMI patients are restricted to specific cell clusters (Fig. 1c). Further, *SAAI* and *SAA2*, two target genes of pro-inflammatory molecules such as IL-1, IL-6, and TNF α ²⁷, are also upregulated in specific subsets of DMI myogenic cells. To further explore this senescent-like phenotype, we compared the different clusters to gene sets related to cellular senescence and SASP production²⁸. Based on this profile, we were able to classify the DMI cells in 3 subpopulations: one subset of fully senescent cells expressing high levels of senescent genes and SASP (clusters 2, 3, 6), one subset of early-senescent cells expressing senescence markers that did not transcribe into SASP cytokine secretion (cluster 4), and one subset non-senescent cells (clusters 0, 1, 5) (Fig. 2a–d). Sample demultiplexing showed that

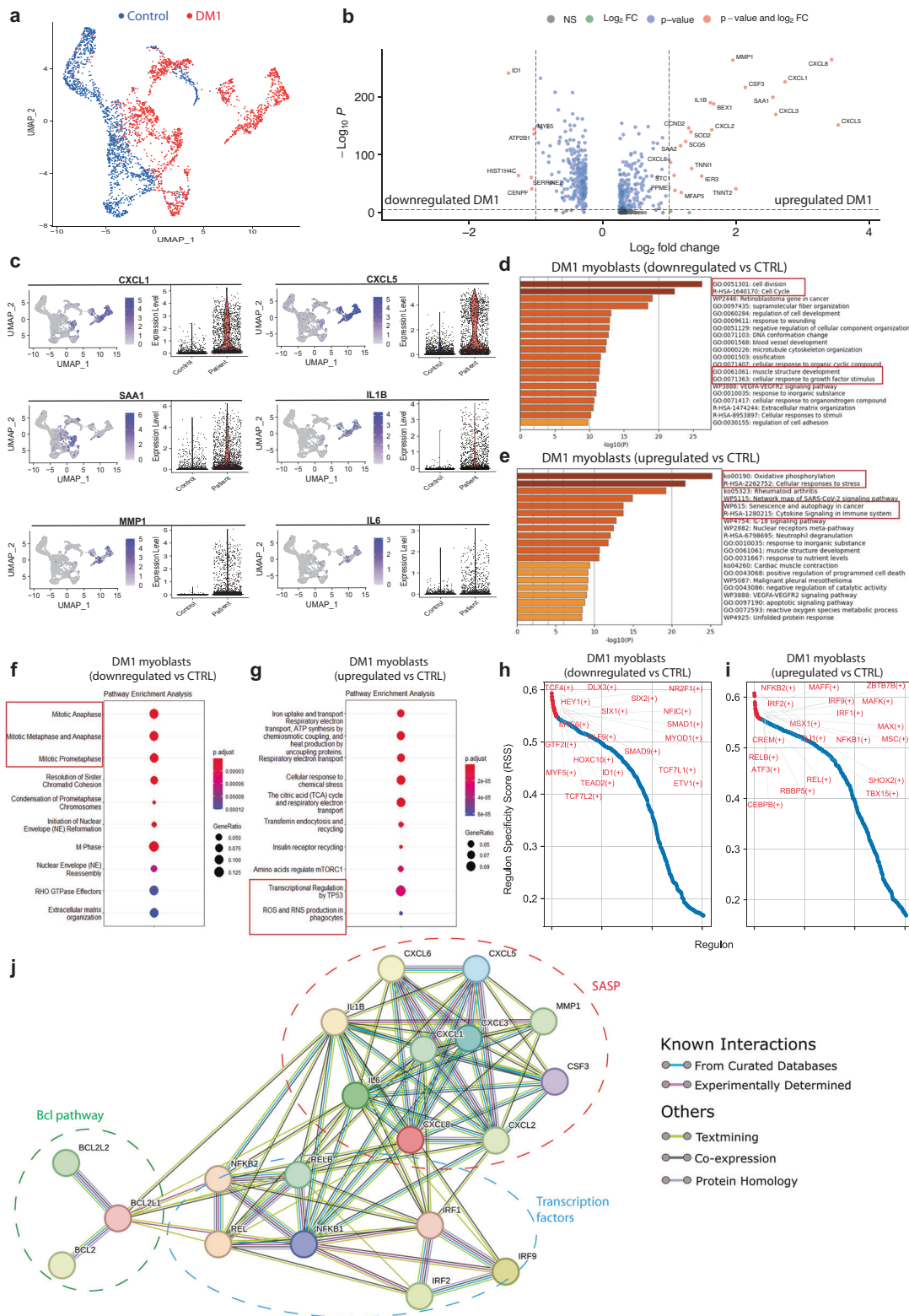


Fig. 1 | scRNA-seq analysis of myogenic cells from control and DM1 patients. **a** UMAP embeddings displaying the control (blue dots) and DM1 patient cell populations (red dots). **b** Volcano plot depicting differentially expressed genes (DEGs) downregulated or upregulated in DM1 patient cells vs controls. The x-axis represents the log₂ of the expression fold change and the y-axis represents the negative log₁₀ of the adjusted *p*-value of the Wilcoxon rank-sum test. Blue dots represent the transcripts that were statistically significant ($P < 10^{-6}$; dotted horizontal line) while red dots represent the top DEGs ($|\log_2FC| > 1.0$; vertical dotted line). **c** Feature and violin plots showing the expression of selected DEGs in DM1 patient and control cells. **d, e** Functional enrichment analysis with GO Biological

Processes analysis using DEGs downregulated (**d**) and upregulated (**e**) in DM1 vs control (CTRL) cells. The X-axis represents the $-\log_{10}(P\text{-value})$. **f, g** Bubble diagram showing the top 10 Reactome pathways for DEGs downregulated (**f**) and upregulated (**g**) in DM1 vs control cells. Vertical axes show enriched terms, and horizontal axes represent the genes in each cluster. Larger node size represents the larger ratio of enriched genes/total genes. **h, i** Rank for regulons for downregulated genes (**h**) or upregulated genes (**i**) in DM1 vs control cells based on regulon specificity score (RSS). **j** STRING analysis showing the interactions between top SASP, transcription factors, and the anti-apoptotic BCL pathway.

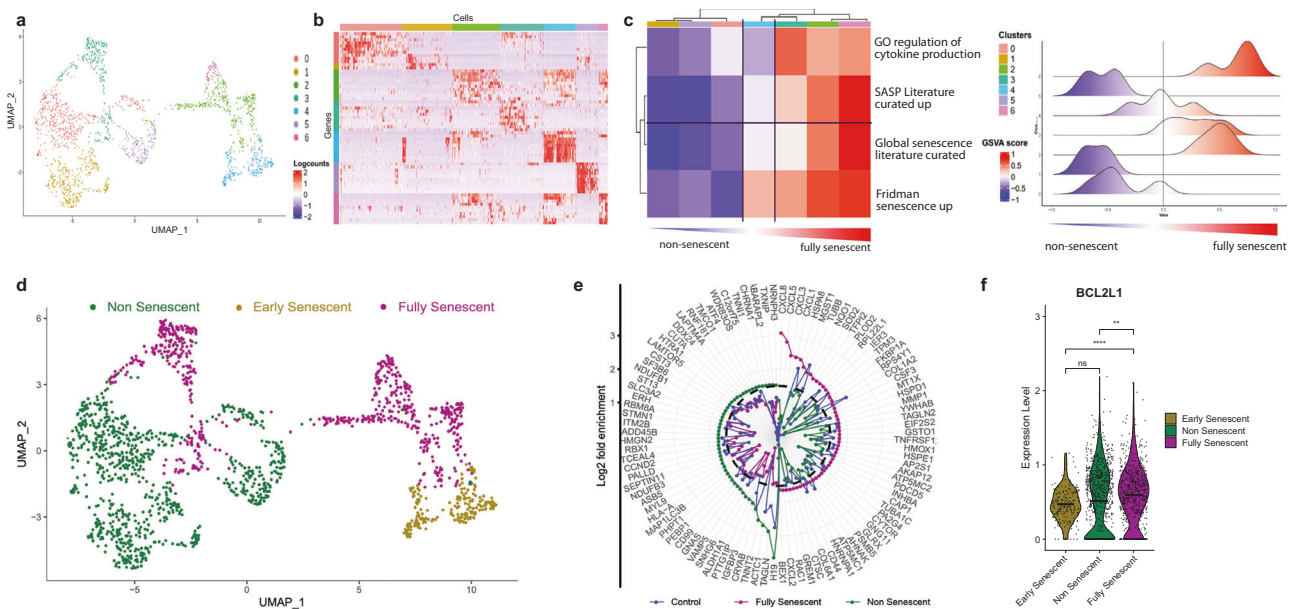


Fig. 2 | Identification of senescent cell subpopulations in samples from DMI patients. **a** UMAP visualization showing unsupervised clustering revealing 7 distinct cell populations in patient cells. **b** Heatmap showing the top differentially expressed genes (DEGs) from each cluster. **c** Heatmap and ridge plots showing the fold change of GSVAs on gene sets related to cellular senescence and cytokine secretion comparing DEGs transcripts from each cluster. Clusters with positive GSVAs for all the gene sets were annotated as fully senescent while clusters with mixed and negative GSVAs scores were annotated as early-senescent and non-

senescent, respectively. **d** UMAP embedding characterizing the fully senescent (purple), early-senescent (gold), and non-senescent populations (green) in patient cells. **e** Radar plot of DEGs of fully senescent, versus non-senescent cells, and control cells (blue). Y-axis represents the \log_2 of the expression fold change. Dotted line delineates the threshold of $\log_2FC = 1.2$. **f** Violin plot showing the expression of *BCL2L1* (BCL-XL) in fully senescent, early-senescent, and non-senescent subpopulations. ** $p = 0.002$, **** $p = 5.9 \times 10^{-8}$ (One-sided Wilcoxon-Mann-Whitney unpaired U test).

there is a high variability across individuals in the percentage of cells that clusters in the senescent cell subpopulation, with the 2 samples from men with high numbers of CTG repeats (954 and 1,200 CTG repeats) having higher proportion of senescent cells (~66% and ~15% senescent cells) compared to the sample from woman with lower number of CTG repeats (554 CTG repeats, ~5% senescent cells) (supplementary Fig. 2f). By comparing the molecular signature of the senescent and non-senescent clusters versus all the combined clusters found in our control sample, we observed a senescent molecular signature present only in the senescent cluster (*CXCL1*, *CXCL3*, *CXCL5*, *CXCL8*, *MMPI1*, *SOD2*); and that the non-senescent cluster in DMI samples expressed a similar molecular profile as our control sample (Fig. 2e). Analysis of the BCL-XL (*BCL2L1* gene) anti-apoptotic pathway showed a higher expression in the fully senescent subpopulation compared to early senescent and non-senescent subsets (Fig. 2f).

Production of SASP by senescent cells varies depending on the cell type and inducer^{29,30}. Thus, we selected all the top differentially expressed genes (>1.7-fold) in DMI and controls samples and we investigated the presence of these genes in the SASP Atlas³⁰, a proteomic database that analyzed the SASP factors secreted by different cell types (fibroblasts and epithelial cells) subjected to multiple senescence inducers (irradiation, oncogene-induced, treatment-induced). These findings indicate that the top genes overexpressed in DMI patients (e.g., *STC1*, *SOD2*, *MMPI1*, *CXCL5*, *CXCL8*) are canonical SASP markers expressed at the protein level by senescent cells, regardless of the cell type or the senescence inducer (Supplementary Fig. 3a). On the other hand, the top upregulated genes in healthy control myoblasts (e.g., *COL3A1*, *TOP2A*) are negative regulators of cellular senescence in the SASP Atlas (Supplementary Fig. 3b).

Cellular senescence is associated with reduced myogenesis in DMI

As single-cell analysis revealed distinct molecular signatures associated with cellular senescence in DMI cells, we further explored how

this process was affected in myogenic cells in vitro and in situ. First, we performed SA- β -Gal assay on myoblasts in vitro, and we observed an 11-fold increase ($p = 0.0023$) in the proportion of β -Gal + senescent cells in patient-derived DMI myoblasts compared to healthy controls (Fig. 3a, b). Further analysis on cultured myoblasts confirmed that *PI6* is significantly upregulated ($p = 0.046$) in DMI cells compared to controls (Fig. 3c). As senescence is characterized by cell cycle arrest, myoblast proliferation was assessed using a live cell imaging system (IncuCyte), and the results showed a significant reduction ($p = 0.042$) in cell proliferation in DMI patients compared to controls (Fig. 3d).

To determine if the accumulation of toxic RNA is associated with cellular senescence in DMI, the number of intranuclear RNA foci was compared in senescent (SA- β -Gal +) and non-senescent (SA- β -Gal-) DMI myoblasts. A 4-fold increase ($p = 0.0017$) in the number of RNA foci per senescent DMI cells was observed compared to non-senescent cells (Fig. 3e, f). The same experiment performed in healthy control cells or in DMI cells treated with RNase revealed the absence of intranuclear RNA foci, both in senescent and non-senescent cells (Supplementary Fig. 4). Considering the oxidative stress signature observed by scRNAseq, the expression of ROS in the senescent vs non-senescent cell subpopulations was also assessed by flow cytometry using the CellROX (ROS marker) and FITC conjugated SA- β -Gal. The results show that senescent cells express a higher level of oxidative stress compared to non-senescent DMI myoblasts (Supplementary Fig. 5).

Thereafter, cellular senescence markers were assessed on flash-frozen skeletal muscle biopsies to determine if senescence is also a feature of the disease in situ. Immunofluorescence staining on the skeletal muscle section showed a 5-fold increase ($p = 0.022$) in the proportion of satellite cells (PAX7+) co-expressing the cell cycle inhibitor P16 (Fig. 3g, h) in DMI muscles compared to controls. Gene expression analysis of skeletal muscle biopsies confirmed a significant upregulation in the expression of the cell cycle inhibitors *PI6* (5-fold; $p = 0.0075$) and *P21* (17-fold; $p = 0.004$) in samples from DMI patients compared to controls (Fig. 3i). Noteworthy, the proportion of

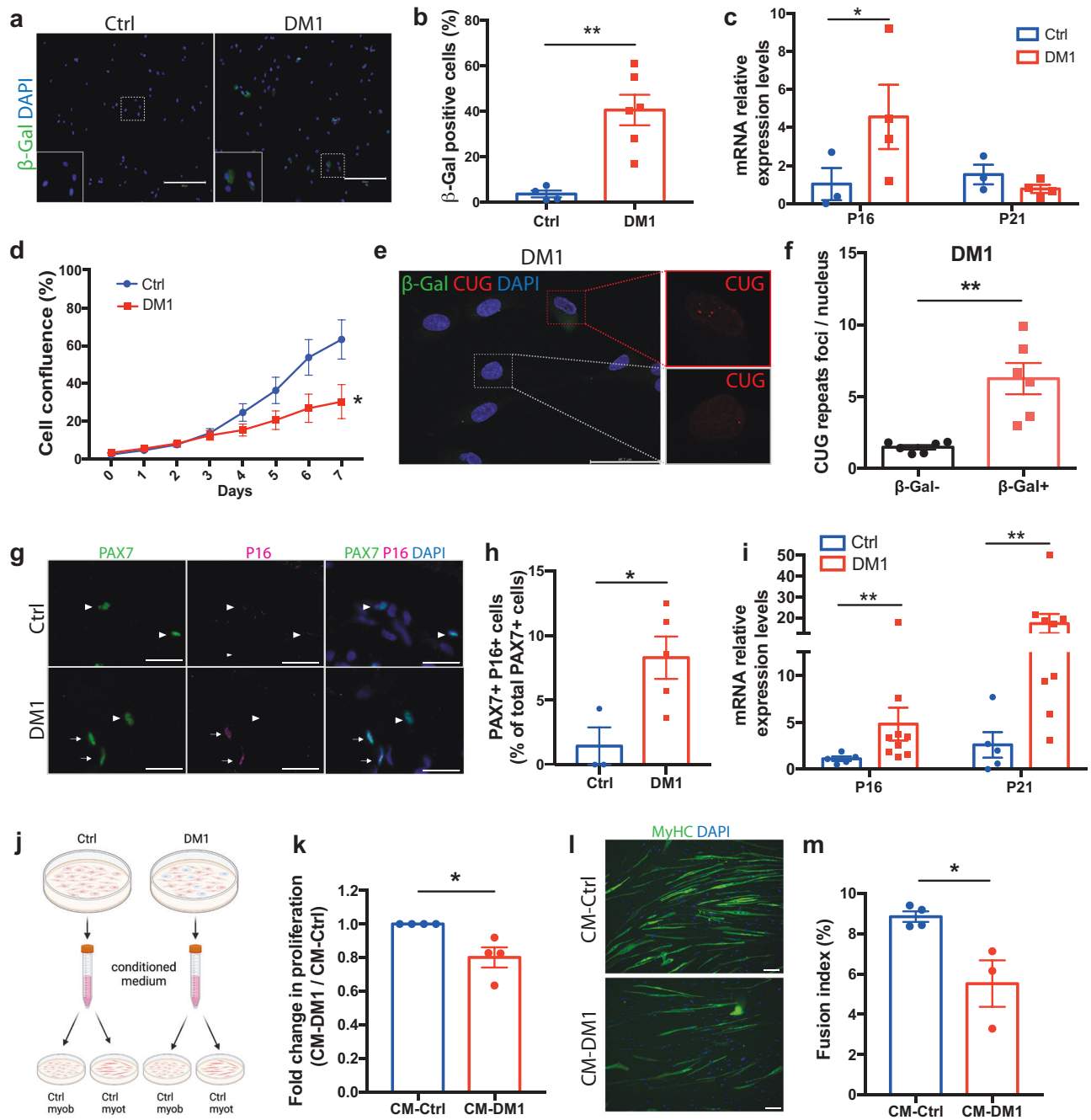


Fig. 3 | MuSC senescence is a hallmark of DMI in vitro and in situ.

a Representative micrographs of control and DMI myoblasts stained for FITC SA-β-Gal (green). Scale bars: 300 μm. **b** Quantification of the percentage of SA-β-Gal+ senescent cells ($n = 4$ ctrl and 6 DMI cell lines; average of 467 cells [257-705 cells] counted per sample) $**p = 0.0023$ (Two-tailed unpaired *T*-Test with Welch's correction). **c** qPCR for the senescence markers *P16* and *P21* in control and DMI myoblasts ($n = 3$ ctrl and 4 DMI cell lines); $*p = 0.046$ (two-way ANOVA followed by Bonferroni's multiple comparisons). **d** Growth curve of control and DMI myoblasts cultured for 7 days ($n = 5$); $*p = 0.042$ (Two-tailed multiple unpaired *T*-test). **e** Representative micrograph of co-immunostaining for RNA FISH (CUG repeats, red), SA-β-Gal (green), and DAPI (blue). Red lines identify a senescent cell and gray dashed lines a non-senescent cell. Scale bar: 46.2 μm. **f** Quantification of the number of intranuclear RNA foci per senescent or non-senescent cell in DMI myoblasts. ($n = 6$ samples; average of 50 cells [22-104 cells] counted per sample) $**p = 0.0017$ (Two-tailed unpaired *T*-test). **g** Co-immunofluorescence labeling of PAX7 (green) and P16 (magenta) on control and DMI muscle sections. White

arrowheads indicate PAX7 + P16+ MuSCs and white arrows indicate PAX7 + P16- senescent MuSCs. Scale bars: 50 μm. **h** Quantification of senescent MuSCs expressing PAX7 and P16 ($n = 3$ Ctrl and 5 DMI biological samples; average of 110 cells [23-246 cells] counted per sample) $*p = 0.0219$ (Two-tailed unpaired *T*-Test with Welch's correction). **i** qPCR for the senescence markers *P16* and *P21* on control and DMI muscle biopsies ($n = 5$ Ctrl and 9 DMI biological samples). $**p = 0.0075$ (*P16*) and $**p = 0.004$ (*P21*) (two-tailed Mann-Whitney test). **j** Schematic showing the experimental design of the conditioned medium (CM) assay. Created with BioRender.com. **k** Cell proliferation of healthy myoblasts treated with control or DMI CM for 4 days ($n = 4$); $*p = 0.0452$ (Two-tailed unpaired *T*-test with Welch's correction). **l** Representative micrographs of myotubes differentiated for 3 days and then cultured with control or DMI CM for 2 days (MyHC in green; DAPI in blue). Scale bars: 50 μm. **m** Fusion index of myotubes treated with control or DMI CM. ($n = 4$ Ctrl and 3 DMI biological samples; average of 860 nuclei cells [576-1376 cells] counted per sample). $*p = 0.0219$ (two-tailed unpaired *T*-test). Data are expressed as means ± SEM. Source data are provided as a Source Data file.

senescent cells is lower in absolute number in MuSCs in vivo compared to myoblasts in vitro, which could be explained by the different markers used (P16 vs SA- β -Gal) or the different myogenic activation states (i.e., quiescent MuSCs in vivo vs proliferating myoblasts in vitro). Analysis of publicly available scRNAseq dataset of MuSCs at the different stages of activation post-injury revealed that *DMPK* expression increases in myogenic cells after injury, suggesting that the accumulation of toxic RNA foci is higher in activated myoblasts than in quiescent MuSCs (supplementary Fig. 6).

SASP production impairs myogenesis in vitro

Considering that the scRNAseq analysis revealed that the senescent cells in DMI display a strong SASP profile, we assessed if the release of paracrine factors by senescent cells could affect non-senescent neighboring cells. The conditioned medium of control and DMI myoblasts was collected and added on healthy control cells (Fig. 3j). The addition of DMI-conditioned medium reduced myoblast proliferation compared to control-conditioned medium (Fig. 3k), indicating that DMI senescent cells blunt myogenesis by their release of harmful paracrine factors. To determine if SASP could also affect multinucleated myotubes, healthy myoblasts were differentiated for 3 days, and then conditioned media was added to the mature myotubes. The results showed a reduction in the fusion index in cells that received the DMI-conditioned medium compared to the healthy control-conditioned medium (Fig. 3l, m).

SASP production is correlated with muscle weakness in DMI patients

To determine the impact of SASP production on muscle function in vivo, blood serum from DMI patients ($n = 103$; Supplementary Table 2) was collected to measure the level of expression of IL-6, a prominent SASP cytokine. Thereafter, the maximum isometric muscle strength of different muscle groups of the lower limb (ankle dorsiflexors, hip flexors, knee extensors, knee flexors) and upper limb (shoulder flexors, shoulder abductors, elbow flexors, elbow extensors) was quantitatively assessed. Using equations that adjust for age, sex, and weight, the predicted strength value of each muscle group was calculated, which allowed to identify a relative deficit compared to normative value³¹. For the lower limb, a significant negative correlation between IL-6 levels and predicted maximal muscle strength was observed for ankle dorsiflexors ($R: -0.426$; $p < 0.0001$), hip flexors ($R: -0.397$; $p < 0.0001$), knee extensors ($R: -0.273$; $p = 0.0055$), and knee flexors ($R: -0.300$; $p = 0.0021$) (Fig. 4a–d). For the upper limb, a significant negative correlation was observed for the shoulder flexors ($R: -0.405$; $p < 0.0001$), shoulder abductors ($R: -0.370$; $p < 0.0001$), elbow flexors ($R: -0.337$; $p < 0.0005$), and elbow extensors ($R: -0.407$; $p < 0.0001$) (Fig. 4e–h).

Thereafter, we separated the group in patients expressing low or high levels of IL-6, based on the normative value for healthy individuals (upper 95th percentile reference limit of healthy individuals: 4.45 pg/ml)³². Twenty-three DMI patients out of 103 (22.3%) had IL-6 levels over the reference limit of healthy individuals, suggesting that IL-6 is abnormally elevated in this population. The average IL-6 level was 3.7-fold higher in the high IL-6 expressing group (7.61 pg/ml) compared to the low IL-6 expressing group (2.04 pg/ml) (Supplementary Table 2). As expected, DMI patients were weaker than normative values for healthy individuals for most muscle groups even if their IL-6 level was low (Fig. 4i, j). However, the DMI patients that express higher levels of IL-6 are significantly weaker compared to those that had a normal SASP profile for all muscle groups tested: ankle dorsiflexors (–18%, $p = 0.006$), hip flexors (–14%, $p = 0.001$), knee extensors (–12%, $p = 0.015$), knee flexors (–12%, $p = 0.021$), shoulder flexors (–22%, $p = 0.006$), shoulder abductors (–16%, $p = 0.016$), elbow flexors (–5%, $p = 0.032$), elbow extensors (–24%, $p = 0.003$) (Fig. 4i, j).

The functional capacity of DMI participants was assessed using standardized physical tests validated in the DMI population: the

Timed-Up and Go (time to rise from a chair, walk 3 meters, walk back and sit down), 10-meter Walk-Test (10mWT; walking speed over a short distance), grip test (maximal hand grip strength), and pinch test (thumb to index pinch strength)^{33,34}. We observed a significant correlation between IL-6 levels and the scores at the Timed-Up and Go ($R: 0.400$; $p < 0.0001$), 10mWT ($R: -0.387$; $p < 0.0001$), grip test ($R: -0.315$; $p = 0.0014$), pinch test ($R: -0.345$; $p < 0.0004$) (Fig. 4k, m, o, q). There was a significant reduction in the group expressing higher levels of IL-6 compared to the one expressing lower levels of IL-6 in the performance at the different functional tests: Timed-up and Go (+1 s [+10%], $p = 0.005$), 10 mWT (–0.15 m/s [–12%], $p = 0.001$), and pinch test (–0.74 kg [–12%], $p = 0.032$) (Fig. 4l, n, p, r).

Further analysis using the stepwise regression model was used to verify if IL-6 is a candidate predictor variable explaining muscle strength and functional outcomes. Results show that IL-6, together with the clinical phenotype, age and/or sex of the patient, is a variable that explains the variance of the scores obtained by participants to the Timed-up and Go (standardized β : 0.18, $p = 0.048$), 10 mWT (standardized β : –0.2, $p = 0.003$), and the predicted maximal muscle strength of hip flexors (standardized β : –0.27, $p = 0.02$), knee extensors (standardized β : –0.20, $p = 0.034$), knee flexors (standardized β : –0.19, $p = 0.034$), ankle dorsiflexors (standardized β : –0.24, $p = 0.005$), shoulder flexors (standardized β : –0.28, $p = 0.002$), shoulder abductors (standardized β : –0.22, $p = 0.009$), elbow flexors (standardized β : –0.18, $p = 0.034$), and elbow extensors (standardized β : –0.206, $p < 0.001$) (Supplementary Table 3).

The same analyses were performed based on the serum level of TNF α . No correlation was observed between TNF α levels and the strength of ankle dorsiflexors, hip flexors, knee extensors, knee flexors, shoulder flexors, shoulder abductors, elbow flexors, elbow extensors, 10mWT, grip test, and pinch test (supplementary Fig. 7). Only the Timed-up and go ($R: 0.270$; $p = 0.006$) showed a correlation with TNF α levels.

Altogether, our findings indicate that cellular senescence and SASP are hallmarks of DMI, which could explain the reduced myogenic capacity and the impaired muscle function. Therefore, we next explored the possibility of eliminating these senescent cells as a potential therapy to alleviate DMI disease progression.

Senolytics specifically eliminate senescent myoblasts in DMI and reduce SASP expression

Considering that the pathophysiological mechanism behind cellular senescence varies depending on the inducers and cell types, we tested the impact of six different senolytics that act through different mechanisms to induce apoptosis of senescent cells: the FOXO4-DRI peptide (p53-FOXO4 interaction), Fisetin (PI3K/AKT pathway), Dasatinib + Quercetin (PI3K/AKT pathway), Navitoclax (BCL-2/BCL-XL inhibitor), A1331852 and A1155463 (Selective BCL-XL inhibitors)^{24,35–38}. Analysis of cell viability following the treatment of myoblasts with different concentrations of senolytics showed that the PI3K/AKT inhibitor Dasatinib + Quercetin, was toxic for cells isolated from both healthy controls and DMI patients (Supplementary Fig. 8). Similarly, Fisetin was toxic for both Ctrl and DMI cells at higher concentrations, although it reduced the cell viability only in the DMI population at specific concentrations (20 and 25 μ m). The FOXO4-DRI peptide eliminated cells in the Ctrl and DMI groups, which is coherent with our scRNAseq data showing that *FOXO4* is not specifically upregulated in the senescent cell population (Supplementary Fig. 9) Navitoclax selectively eliminated cells in DMI samples at a specific concentration (3 μ m); however, A1155463 was the most effective to target cells specifically in the DMI group and not affect the healthy cell viability (Fig. 5a). These results are consistent with the scRNAseq dataset showing an upregulation in *BCL2L1* (gene encoding for BCL-XL) expression in the fully senescent cell subset (Fig. 2f). Moreover, A1155463 was effective at a lower concentration, in the nanomolar

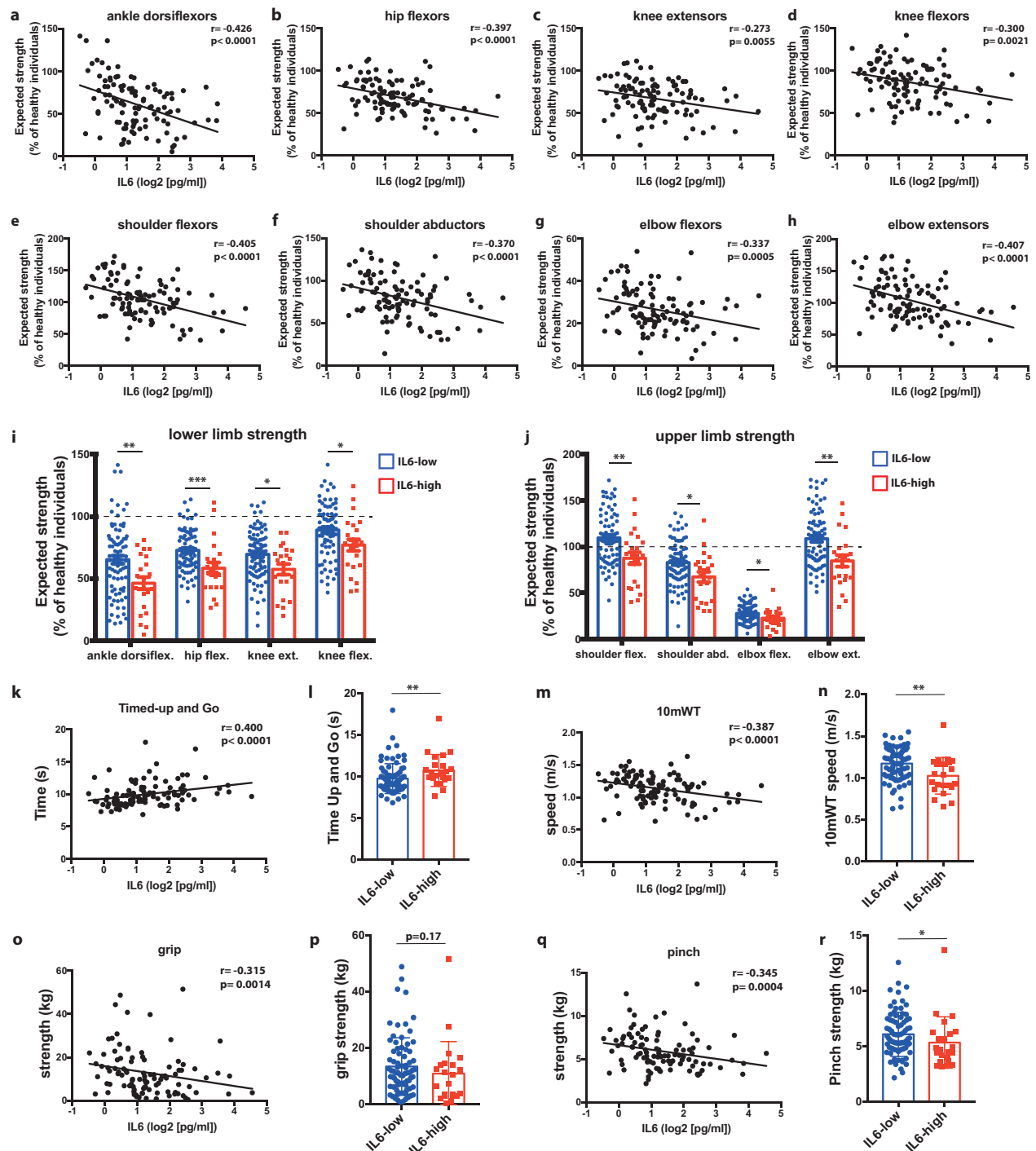


Fig. 4 | SASP expression is negatively correlated with muscle strength and functional outcomes in DMI. a–d Correlation between serum IL-6 levels in DMI patients and the expected strength (relative to normative values) of different muscle groups of the lower limb (ankle dorsiflexors, hip flexors, knee extensors, knee flexors) and **e–h** upper limb (shoulder flexors, shoulder abductors, elbow flexors, elbow extensors). **i, j** Expected muscle strength of DMI patients with low or high levels of IL-6 (based on a cut-off reference limit for healthy individuals of 4.45 pg/ml) for the lower limb (**i**) and upper limb (**j**) muscle groups. Dashed line indicates the normative data for isometric muscle strength in healthy individuals of

the same age, sex, and weight. **k, m, o, q** Correlation between serum IL-6 levels in DMI patients and the results of different functional capacity tests: Timed-up and Go, 10-meter walk test (10mWT), grip test, pinch test. **l, n, p, r** Functional capacity test results for DMI patients with low or high levels of IL-6 levels. **i, j, l, n, p, r** Data are expressed as means \pm SEM. $n = 103$ patients (80 patients IL-6 low, 23 patients IL-6 high). $*p < 0.05$, $**p < 0.01$, $***p < 0.001$ (Panels **a–h, k, m, o, q**: Spearman ρ correlation coefficient and two-tailed p -value. Panels **i, j, l, n, p, r**: Two-tailed Mann–Whitney U test). Source data are provided as a Source Data file.

range. Therefore, this lead compound was chosen for the following experiments. To confirm that A1155463 induced apoptosis of senescent cells, an Annexin V/propidium iodide (PI) assay was performed on healthy and DMI myoblasts. Treatment of myoblasts with A1155463 at a dose of 100 nM increased cell apoptosis only in the DMI samples

(Fig. 5b, c). SA- β -Gal staining on DMI or controls myoblasts treated with vehicle or A1155463 showed a significant reduction in the number of SA- β -Gal $^{+}$ senescent cells in the A1155463-treated DMI group (Fig. 5d, e). Further analysis of senescence gene expression demonstrated that A1155463 treatment reduced *P16* expression in

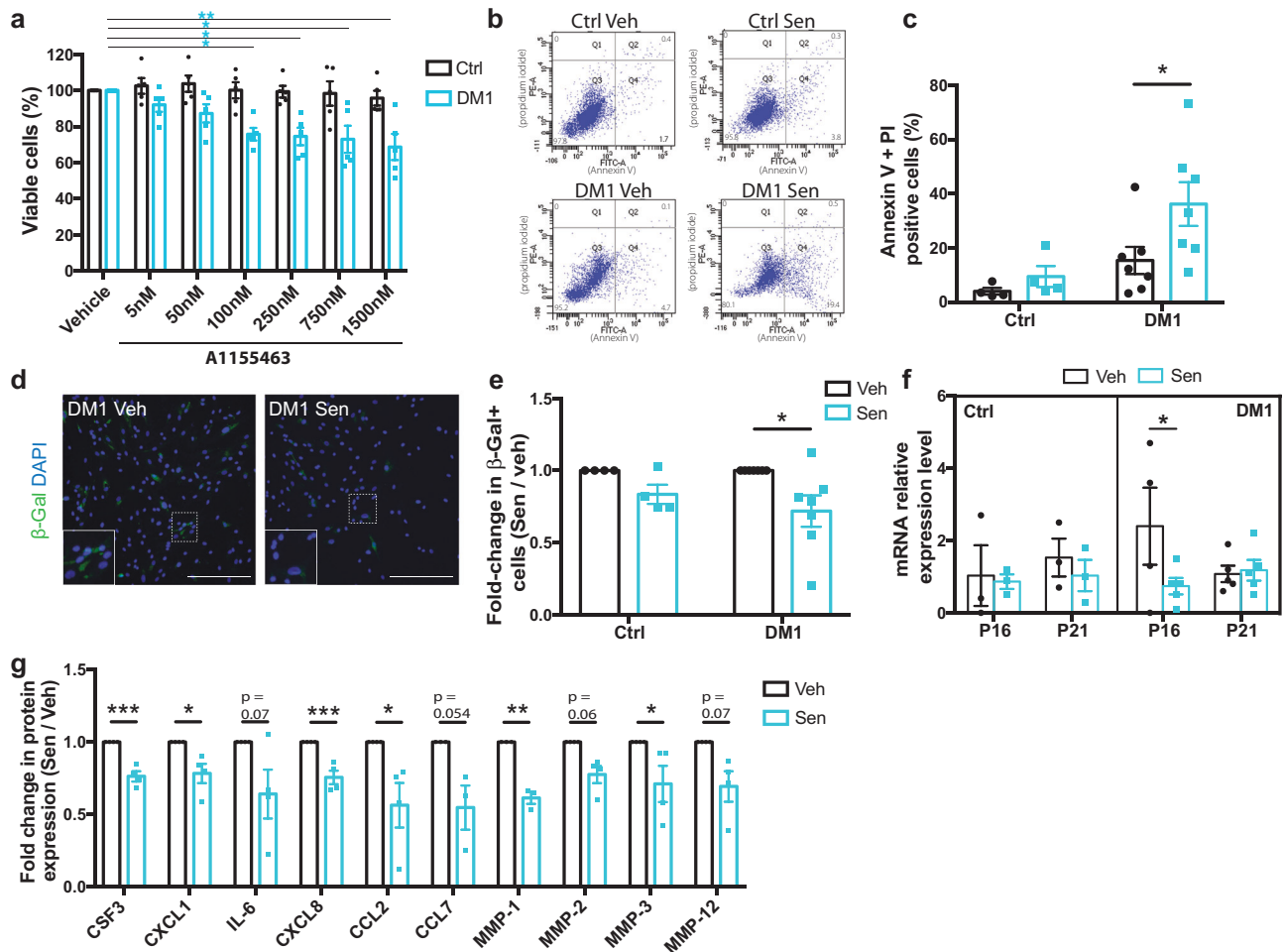


Fig. 5 | A1155463 shows senolytic activity on DMI primary myoblasts culture.

a Cell viability assay of A1155463 at different concentrations using control (Ctrl) and DMI patients' myoblasts ($n = 5$). * $p = 0.038$ (100 nM), * $p = 0.023$ (250 nM), * $p = 0.011$ (750 nM), ** $p = 0.0016$ (1500 nM) (two-way ANOVA with Tukey's multiple comparisons test). **b** Representative FACS plots of Annexin-V (FITC) and propidium iodide (PE), and **c** quantification of the percentage of positive apoptotic/necrotic cells after 48 h treatment of myoblasts (DMI and Ctrl) with 100 nM of A1155463 (Sen) or with vehicle (Ctrl), ($n = 4$ Ctrl and 7 DMI cell lines); * $p = 0.034$ (one-way ANOVA with Sidak's multiple comparisons test). **d** Representative micrographs of DMI myoblasts stained for the senescent marker SA- β -Gal (green) after 72 h treatment with 100 nM of A1155463 or with vehicle. Scale bar: 300 μ m. **e** Quantification of the number of SA- β -Gal+ cells expressed as fold change ratio of A1155463-treated (Sen)

versus non-treated (Veh) cells ($n = 4$ Ctrl and 7 DMI cell lines; average of 1064 cells [142-2873 cells] counted per biological sample). * $p = 0.015$ (one-way ANOVA with Sidak's multiple comparisons test). **f** Quantitative real-time PCR for the senescence markers *P16* and *P21* on primary myoblasts after 72 h of treatment with vehicle or A1155463 ($n = 3$ Ctrl and 5 DMI cell lines, except $n = 4$ for the p16 expression of DMI-Veh group). * $p = 0.042$ (two-way ANOVA with Tukey's multiple comparisons test). **g** Multiplex Luminex assay of SASP factors showing fold change ratio of A1155463-treated (Sen) versus non-treated (Veh) DMI myoblasts ($n = 4$ cell lines, except $n = 3$ for CCL7 and MMP-1 expression). *** $p = 0.0005$ (CSF3), * $p = 0.018$ (CXCL1), *** $p = 0.002$ (CXCL8), * $p = 0.041$ (CCL2), ** $p = 0.009$ (MMP-1), * $p = 0.027$ (MMP-3) (two-tailed multiple unpaired *T*-tests). Data are expressed as means \pm SEM. Source data are provided as a Source Data file.

DMI samples, but not in controls (Fig. 5f). The expression of SASP factors was analyzed by multiplex Luminex assay in DMI cells treated with A1155463 or vehicle. Results showed that senolytic treatment significantly reduced the expression of many SASP factors such as CSF3 ($p = 0.0005$), CXCL1 ($p = 0.018$), CXCL8 ($p = 0.002$), CCL2 ($p = 0.041$), MMP1 ($p = 0.009$), and MMP3 ($p = 0.027$) (Fig. 5g). A trend toward reduction was also observed for IL-6 ($p = 0.078$), CCL7 ($p = 0.054$), MMP2 ($p = 0.06$), and MMP12 ($p = 0.07$). On the other hand, growth factors that stimulate cell proliferation such as EGF ($p = 0.0005$) and FGF2 ($p = 0.046$) were increased by A1155463 treatment (Supplementary Fig. 10). Other anti-inflammatory cytokines and growth factors such as IL-4 ($p = 0.18$), IL-13 ($p = 0.12$), FLT-3L ($p = 0.24$), and VEGF-A ($p = 0.36$) were not significantly affected by the treatment (Supplementary Fig. 10).

The eradication of senescent cells restores myogenesis in DMI

Next, we aimed to determine if the elimination of senescent cells, and the associated reduction in the expression of SASP factors, in

A1155463-treated DMI myoblasts restores the myogenic potential of the non-senescent cells. Myoblasts were treated with A1155463 or vehicle for 1 day and were allowed to recover in proliferating media for 3 days. Immunostaining for the proliferation marker Ki67 revealed that A1155463-treatment increased the proportion of Ki67+ cells in the DMI samples (1.8-fold increase), but not in the controls (Fig. 6a, b). To determine if this rescue on cell proliferation was attributable to the reduction in the SASP, the media from senolytic-treated or untreated DMI myoblasts was collected and added on healthy control myoblasts. After 5 days, a higher number of cells was observed in the senolytic-treated conditioned medium group compared to the untreated conditioned medium group (Fig. 6c), suggesting that the senolytic-induced reduction in harmful SASP rescues myoblast proliferation.

In another set of experiments, myoblasts were treated with A1155463 or vehicle for 1 day and incubated in a low-serum differentiating medium for 5 days. Immunofluorescence staining for the differentiating marker MYOG revealed a significant increase (2.2-fold) in the proportion of MYOG+ cells only in the DMI samples, and not in

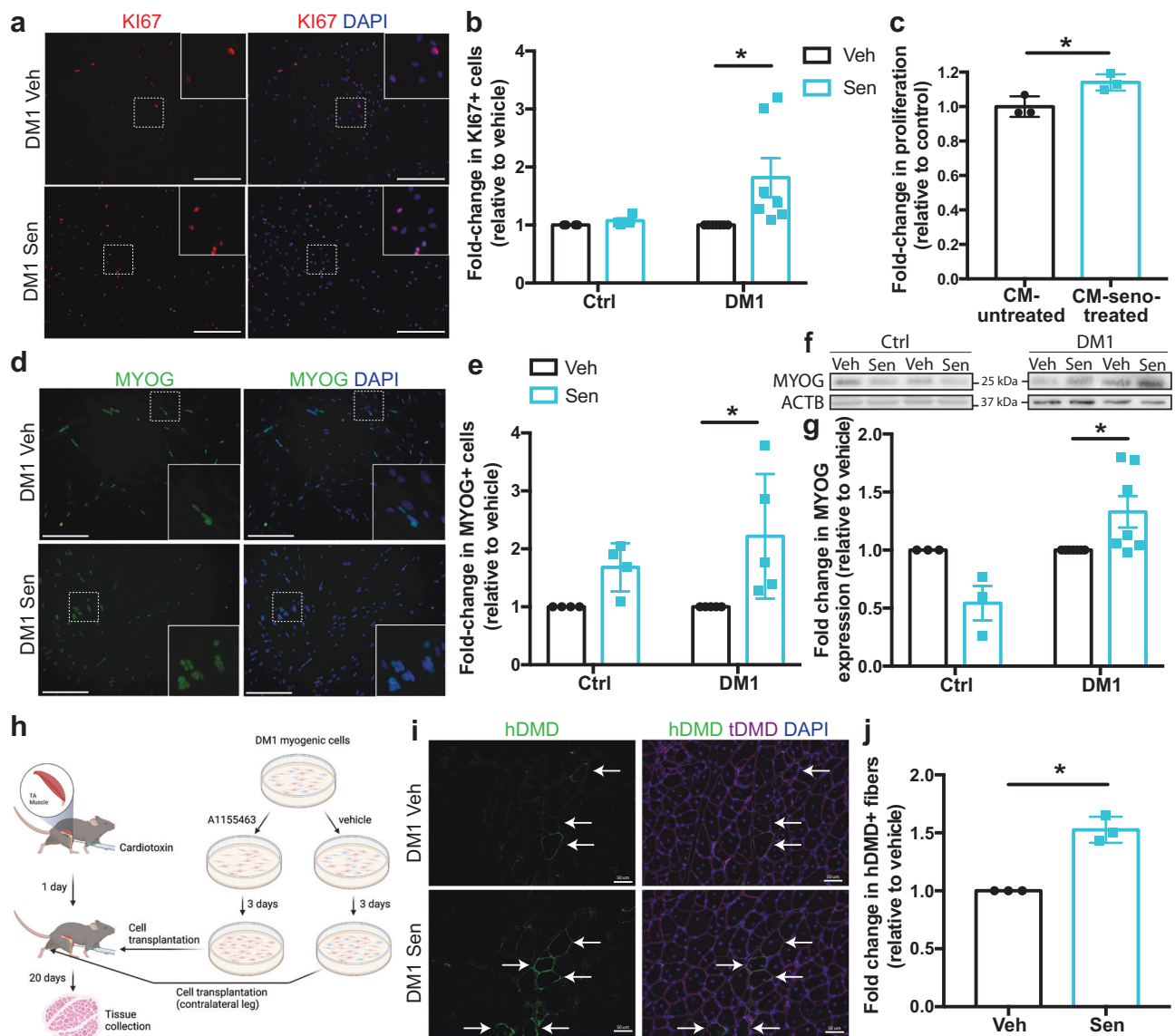


Fig. 6 | Clearance of senescent cells in DM1 improves myogenesis in vitro and in vivo. **a** Representative micrographs of DM1 myoblasts immunolabeled with KI67 (red) after 72 h of treatment with vehicle (Veh) or A1155463 (Sen). Scale bars: 300 μ m. **b** Quantification of the proportion of KI67+ cells treated with A1155463 (Sen) relative to vehicle ($n = 4$ Ctrl and 7 DM1 cell lines; average of 1064 cells [142–2873 cells] counted per sample). $*p = 0.017$ (one-way ANOVA with multiple comparisons). **c** Cell proliferation of healthy myoblasts cultured with conditioned media (CM) from DM1-untreated or DM1-senolytic-treated myoblasts for 5 days; ($n = 3$ biological samples). $*p = 0.033$ (Two-tailed unpaired *T*-test). **d** Representative micrographs of DM1 myoblasts differentiated for 5 days after treatment with vehicle (Veh) or A1155463 (Sen) and immunolabeled with MYOG (green). Scale bars: 300 μ m. **e** Quantification of the number of MYOG+ cells treated with A1155463 (Sen) relative to vehicle ($n = 4$ Ctrl and 5 DM1 cell lines, average number of 1388 cells [104–4218 cells] counted per sample) $*p = 0.0134$ (one-way ANOVA with multiple comparisons). **f** Representative Western blots showing the expression of MYOG in control and DM1 myoblasts differentiated for 5 days after treatment with vehicle

(Veh) or A1155463 (Sen). **g** Quantification of MYOG expression by Western blot (relative to β -actin as loading control). Data are expressed as fold change relative to non-treated (Veh) cells ($n = 3$ Ctrl and 7 DM1 cell lines). $*p = 0.039$ (two-way ANOVA with Sidak's multiple comparisons test). **h** Schematic representation of DM1 myoblast transplantation experiment. Created with BioRender.com. **i** Representative micrographs of muscle sections of TA muscles (21 days post-cardiotoxin injection) of NSG mice transplanted with DM1 myoblasts treated with vehicle (upper images) or A1155463 (bottom images). Sections were immunostained with human dystrophin (hDMD; green), total dystrophin (tDMD, magenta), and DAPI (nuclei, blue). White arrows indicate myofibers expressing hDMD and tDMD. Scale bars: 50 μ m. **j** Quantification of the number of myofibers expressing hDMD in transplanted cells treated with A1155463 (Sen) relative to vehicle ($n = 3$ different DM1 cell lines transplanted in three different mice per cell line; average number of 3388 myofibers [2100–5140 myofibers] counted per biological sample). $*p = 0.014$ (Two-tailed unpaired *t*-test with Welch's correction). Data are expressed as means \pm SEM. Source data are provided as a Source Data file.

the controls (Fig. 6d, e). This increase in MYOG expression in the DM1 samples was also confirmed by Western blot (Fig. 6f, g and supplementary Fig. 11).

To better address the myogenic potential of DM1 myoblasts treated with A1155163 in vivo, we performed a cell transplantation assay. Three different DM1 myoblast lines were treated with A1155463 (100 nM for 24 h) or vehicle and the cells were allowed to recover in

proliferating media for 3 days. These cells were transplanted into the tibialis anterior muscle of NSG mice (3 mice per cell line) that were injured by cardiotoxin (CTX) injection 1 day before. Regenerated TA muscles were collected 21 days post-CTX injection (Fig. 6h). Cell engraftment was assessed by co-immunolabeling for the human dystrophin protein (hDMD) and total dystrophin protein (tDMD) (Fig. 6i). We observed that A1155463 enhanced DM1 cell engraftment by 50%

when compared to the vehicle (Fig. 6j). Taken together these results indicate that A1155463 treatment can significantly improve the myogenic potential of DMI myoblasts in vivo.

Discussion

Our findings demonstrate that cellular senescence is a hallmark of myogenic cells in DMI. Using single-cell transcriptomics and multiplex Luminex assay, we show that a subset of these cells displays a molecular signature characterized by high levels of expression of SASP factors. Our findings show that IL-6, a ubiquitous SASP factor, is associated with muscle weakness and functional limitations in DMI patients. By screening for different senolytics, we identify a lead molecule, A1155463, that specifically eliminates senescent cells in DMI. The senolytic-induced reduction of SASP is associated with a restoration of the myogenic potential of DMI myoblasts in vitro and in vivo. Altogether, these findings provide insights on the pathophysiology of DMI and identify a therapeutic avenue for the treatment of this disease (Supplementary Fig. 12).

Signs of cellular senescence have been observed previously in cells isolated from skeletal muscles of DMI patients; however, these studies used a mixed population of cells that were not purified by FACS and they did not validate if these senescence markers are co-expressed with myogenic cell markers^{11–13}. Therefore, it was not possible to clearly delineate if myogenic cells, or other cell types, were becoming senescent. Among the different cell types, fibroblasts or mesenchymal stromal cells have been characterized as a predominant senescent cell type in various pathogenic conditions³⁹. A recent study showed that fibroblasts derived from DMI patients have impaired DNA damage response, reduced proliferation, and exhibit signs of premature senescence⁴⁰. However, single-cell RNAseq datasets (e.g. Human Protein Atlas) showed that the *DMPK* gene is predominantly expressed in myogenic cells compared to any other mononucleated cell types in the skeletal muscle, suggesting that this cell type might be more prone to RNA-mediated toxicity^{41,42}. Therefore, we used FACS-purified myogenic cells and we have confirmed that different senescence markers are specifically expressed in a subset of DMI myoblasts. In addition to the in vitro experiments, the co-staining for P16-positive cells and PAX7 on skeletal muscle biopsies revealed the presence of senescent MuSCs in situ, which has never been described before. These findings indicate that cellular senescence in DMI is not only an in vitro artefact caused by replicative stress, but a relevant pathophysiological process of the disease. Furthermore, our experiments were performed on samples from individuals with the infantile, juvenile, or adult form of the disease, while previous studies focused exclusively on the more severe congenital form, suggesting that cellular senescence is a hallmark of the disease no matter the clinical form^{12,43}.

Our findings show that the accumulation of RNA foci is higher in the nuclei of senescent DMI myoblasts compared to non-senescent DMI myoblasts. This association suggests that RNA-mediated toxicity could contribute to the initiation of cellular senescence; however, we cannot exclude that a different mechanism triggers cellular senescence, which in turn leads to CUG repeat foci accumulation. Our transcriptomics findings indicate that there is an enrichment for genes related to oxidative stress, which is coherent with our in vitro findings showing that senescent cells express higher levels of ROS than non-senescent cells. Toxic RNA accumulation caused by the CTG repeats in the *DMPK* gene has been shown to induce ROS production and oxidative damage in DMI^{14,44–47}. Chronic ROS production triggers a DNA damage response leading to cell cycle arrest and cellular senescence, which in turn secretes further ROS and SASP leading to a feed-forward cycle^{14,48,49}. Using C2C12 cells it was shown that the insertion of CUG repeats increases ROS production, which is further exacerbated by H₂O₂ exposure, suggesting that DMI cells produce more ROS and are more sensitive to oxidative stress¹⁴. Analyses from other datasets also show an increase in ROS-producing genes (e.g., *NOX4*) and a decrease

in antioxidant genes (e.g. *SOD3*)^{14,50}. Notably, the expression of antioxidant genes such as *SOD1*, *SOD2*, and *GPX1* have been positively associated with muscle strength in another DMI transcriptomic dataset, suggesting that antioxidant levels could help protect against senescence-associated muscle wasting⁵¹. Overall, our findings and others suggest that RNA-mediated toxicity and oxidative stress could contribute to cellular senescence in DMI myoblasts.

Other transcriptomics datasets have been generated on DMI tissues and cells (reviewed in ref. 52). A study on DMI myogenic cells showed that the transcriptional changes are more important in DMI myoblasts than myotubes⁵⁰. GO term analysis showed that the biological processes that are mostly enriched in DMI myoblasts are signaling pathways, ECM components, and cytoskeletal organization⁵⁰. Another RNAseq dataset performed on human embryonic stem cells (DMI and controls) differentiated into myogenic cells showed that inflammatory pathways such as IL6-JAK-STAT3 signaling are over-expressed in DMI cells, which is coherent with the inflammatory signature that we observed⁵³. Similarly, RNAseq analysis performed on isogenic myoblasts containing or not a CTG₂₆₀₀ expansion showed an enrichment in biological processes such as cellular response to IFN γ ⁵⁴. Using a model of C2C12 cells containing expanded CUG repeats, it was also shown that toxic RNA expression induces a senescence-like signature characterized by enrichment in genes related to ECM organization, response to oxygen levels, apoptosis, and regulation of cell growth¹⁴. Transcriptomic analysis on skeletal muscle samples from individuals with the congenital form of DMI showed a signature very similar to our scRNAseq dataset characterized by downregulation in myogenesis genes and upregulation in inflammatory genes, such as the IL6/STAT3 target genes *SAAI* and *SAA2*⁴³. Moreover, supporting our results, RNAseq on muscle samples from DMI patients and controls showed that genes related to SASP factors (e.g. *CXCL14*, *CXCL16*, and *MMP2*) or cell cycle inhibitors (e.g. *CDKN1A*, *TP63*)⁵⁵, are negatively correlated with muscle strength in DMI⁵¹. Notably, recent findings from DMI patients' transcriptomic response to strength training showed that *CDKN1A* is one of the few genes that is correlated to clinical benefits (i.e., the individuals that experienced greater clinical benefits from strength training showed a stronger reduction in *CDKN1A* expression)⁵⁶. RNAseq performed in other tissues such as the frontal cortex showed an enrichment in inflammatory genes compared to healthy individuals, suggesting that the pro-inflammatory signature is a common feature in different DMI tissues⁵⁷. These findings bring important insights on the molecular mechanisms in DMI, however, bulk RNAseq analysis limits the interpretations regarding the sub-population of cells affected. Particularly, it is not possible with these datasets to determine if the inflammatory signature is generalized or circumscribed to a specific subset of cells, which is especially important in the context of cellular senescence.

To assess the specific molecular signature of myogenic cells in DMI, we used an unbiased approach through scRNAseq. This is the first single-cell transcriptomics dataset generated in DMI⁵². This dataset allowed the identification of specific cell clusters expressing different levels of senescence markers leading to a better comprehension of the different stages of senescence in myoblasts of patients with DMI. Particularly, we identified a specific cluster of DMI myoblasts expressing high levels of SASP factors, while another cluster expressed higher levels of *SAAI* and *SAA2*, two molecules that are triggered by SASP factors and can further stimulate SASP expression by a positive feedback loop^{27,58}. These findings suggest that the expression of SASP by senescent cells have paracrine effects on bystander cells. SASP can promote the senescence profile of surrounding cells, a process called secondary senescence⁵⁹. In addition to MuSCs, SASP could also target post-mitotic cells such as mature myofibers. It was shown using an intraperitoneal transplantation assay of senescent preadipocytes that the systemic secretion of SASP induces muscle atrophy and weakness²⁴. Moreover, the transplantation of

senescent fibroblasts in the skeletal muscle induces a senescence-like phenotype (characterized by signs of DNA damage) in the myonuclei of neighboring myofibers that is associated with fiber atrophy⁶⁰. These findings are consistent with our conditioned medium assay showing that SASP can target multinucleated myotubes and impair their fusion.

The single-cell transcriptomics analysis also revealed that, while a subset of cells shows a fully senescent or early senescent profile, there is a significant proportion of cells that had a similar molecular profile as the one found in our control samples from healthy individuals. These results suggest that elimination of the senescent myoblasts could restore the myogenic activity of non-senescent DM1 myoblasts. Several studies used this approach to alleviate chronic and degenerative diseases in which senescence contributes to the progression of the disease (reviewed in ref. 61,62). By testing different senolytic drugs, we observed that DM1 senescent myoblasts were particularly responsive to inhibitors targeting the BCL family members. Navitoclax (ABT-263; BCL2/BCL-XL inhibitor) was effective at targeting senescent myoblasts in DM1, similar to what was shown in an aging model³⁸; however, the highest efficiency was achieved with the BCL-XL inhibitor A1155463. These results are in accordance with our scRNAseq analysis showing that the SASP factors activate the NF- κ B pathway that binds to the promoter region of the BCL-XL gene⁶³. This is also consistent with our findings showing that BCL-XL gene expression is upregulated specifically in the senescent cell subpopulation. At the opposite, the *FOXO4* gene is not upregulated in the senescent cell subpopulation, which could explain why the FOXO4-DRI senolytic is not specific for this population. Moreover, other senolytics targeting the AKT1/PI3K tested such as dasatinib + quercetin are toxic for both senescent DM1 myoblasts and healthy control cells, which suggests that this pathway is critical for myogenic cell viability. Other studies showed that AKT/PI3K inhibitors strongly impairs myogenic cell function in control cells^{64–66}. Overall, the senescent molecular signature expressed in DM1 myoblasts is distinct to this cell type/inducer and it requires precise molecular targeting to specifically eliminate these cells.

Our findings demonstrate that IL-6, a main component of the SASP cocktail, is correlated with muscle weakness and functional capacity limitations in DM1. These results are consistent with previous observations showing that members of the IL-6 signaling pathway are correlated with signs of histological degenerative changes in the congenital form of the disease⁴³. On the other hand, our findings show that another pro-inflammatory cytokine, TNF α , was not correlated with muscle weakness. These results are consistent with our scRNAseq data showing an increase in the expression of *IL6* but not *TNF* in samples from DM1 patients. These results suggest that there is a specific SASP signature associated with muscle weakness in DM1, and not only a generalized pro-inflammatory profile. Similarly, another study screened for 20 pro-inflammatory cytokines in the serum of patients affected by facioscapulohumeral muscular dystrophy and identified IL-6 as the only cytokine correlating with muscle weakness and disease severity⁶⁷. These findings suggest that IL-6 is a promising biomarker to determine the severity of muscle dysfunction in DM1⁶⁸.

Our results also suggest that targeting SASP cytokines such as IL-6 is a valid therapeutic approach to mitigate disease progression. Our findings show that conditioned medium from DM1 myoblasts contains paracrine factors that negatively impacts cell proliferation. The specific elimination of senescent DM1 myoblasts leads to a reduction in the expression of SASP molecules and restores the myogenic potential of non-senescent DM1 myoblasts through an improvement of their cellular proliferation and differentiation capacity. These results are consistent with a previous study showing that the secretion of SASP by senescent cells blocks myoblast differentiation *in vitro*⁶⁹. The improvement in myogenesis was not observed in cells from healthy individuals, which confirms that the senolytic drug targets a specific pathophysiological mechanism in DM1.

MuSC defects and cellular senescence have been poorly investigated *in vivo*. Despite the intensive efforts directed toward the development of DM mouse models, they all have limitations that do not perfectly mimic the multisystemic nature and the heterogeneity of the disease⁷⁰. Some animal models such as the DM5/DM200 (5-200 CTG repeats) have a low number of CTG repeats⁷¹, while others such as DMSXL (>1000 CTG repeats)⁷² and EpA960/TREDT960I (960 CTG repeats)⁷³ have large expansion. The large range of CTG repeats length (59-2000) presented by the participants included in this study suggests that similar results could be obtained in different mouse models expressing toxic RNA in myoblasts (DMSXL, EpA960, and DM5/DM200). In accordance with our findings, a recent study showed that the induction of the transgene in DM200 mice reduces *Pax7* expression, depletes the MuSC pool, and impairs muscle regeneration⁷⁴; however, whether these defects are triggered by cellular senescence is unknown. Further studies are needed to determine if the stronger muscle wasting and weakness phenotype in mouse models carrying large expansion could be related to higher levels of cellular senescence and SASP. Alternatively, in the HSA^{LR} mouse model, the expression of the transgene is driven by human skeletal alpha actin and the toxic RNA is only expressed in the myofibers⁷⁵. Therefore, this model would not be expected to exhibit significant cellular senescence due to the absence of the transgene in the MuSC population. Notably, these mice were shown to develop severe histopathologic signs (e.g., centronucleated fibers, atrophic fibers), however, they do not develop significant muscle wasting and weakness over time, suggesting that the unaffected MuSCs could be able to compensate for myofiber defects⁷⁵. Overall, our findings using human biological material could help to partially explain the phenotype in the different mouse models of DM1, which will be useful for therapeutic development.

Overall, this study describes a well-defined senescent molecular signature in DM1 myogenic cells, which brings insights on the pathophysiological mechanisms of the disease. Particularly, it identifies the production of SASP as a major characteristic of DM1 myoblasts, which is associated with muscle weakness in DM1. We demonstrated that specific drugs can be used to specifically target these senescent cells and induce their apoptosis, thereby reducing the expression of harmful SASP molecules, which restores the regenerative capacity of neighboring myogenic cells. These findings open a therapeutic avenue that could help to mitigate the impact of DM1, a disease for which no treatment currently exists to slow symptoms progression⁷⁶.

Methods

Participants' recruitment

Convenience sampling was used to recruit the participants. For the experiments on blood inflammatory markers and physical tests (Fig. 4) one hundred and three DM1 participants were recruited as part of an observational study between 2002-2004 (see Supplementary Table 2 for patient characteristics). This study was approved by the Ethics review board of the Centre intégré universitaire de santé et de services sociaux du Saguenay–Lac-Saint-Jean, Canada (#2001-032) in accordance with the principles of the declaration of Helsinki. Participants received compensation for their participation in the study. Written informed consent has been obtained from participants for publication of the research findings. For the experiments involving muscle biopsies, the DM1 patients were recruited in 2019 from the list of patients followed at neuromuscular clinics and healthy individuals were recruited among the friends/family members of the participants or team members (see Supplementary Table 1 for participants' characteristics). Patients were first asked by the nurse of the clinic if they are interested to participate in a research project. The ones that accepted were contacted by the research team. Inclusion criteria for DM1 participants were to be aged over 18-year-old and have a genetically confirmed diagnosis of DM1. Ten DM1 patients and seven healthy individuals were recruited in 2019 and underwent a muscle biopsy.

Biological sex was considered in the study design. Men and women were recruited for this study. The biological sex was assigned (not self-reported). Gender-based analysis was not performed considering that the experiments were mostly carried out in vitro. This study was approved by the Ethics review board of the Centre intégré universitaire de santé et de services sociaux du Saguenay–Lac-Saint-Jean, Canada (#MP-04-2020-6), in accordance with the principles of the declaration of Helsinki. Participants received compensation for their participation in the study. Written informed consent has been obtained from participants for publication of the research findings.

Muscle strength, functional capacity assessments, and blood sample collection

A blood sample was taken from each of the 103 DMI participants recruited in the 2002-2004 observational study and the level of TNF- α and IL-6 was measured at the *Centre de recherche sur les maladies lipidiques* of the *Centre hospitalier de l'Université Laval* (Québec, Canada). DMI patients were classified in a low or high IL-6 expressing group based on the cut-off value representing the upper 95th percentile value for healthy individuals (4.45 pg/ml)³². The maximum isometric muscle strength of the ankle dorsiflexors, hip flexors, knee flexors, knee extensors, shoulder flexors, shoulder abductors, elbow flexors and elbow extensors was assessed using quantitative muscle testing according to a standardized protocol⁷⁷. Muscle strength was expressed as the expected muscle strength of healthy individuals based on a French isometric strength normative database using predictive equations taking into consideration age, sex, and weight of the patients³¹. Patients were subjected to a battery of validated functional tests^{78,79}. Timed-up and Go: time to stand up, walk three meters, turn and walk back to sit down on the chair; 10mWT: comfortable walking speed (m/s) along a 10-meter distance; grip test: maximal grip strength (kg) using a Jamar hand dynamometer; Pinch test: measured using a B&L pinch gauge (kg). All tests were conducted under the supervision of a trained physiotherapist.

Muscle biopsy

A biopsy of the vastus lateralis at the mid-thigh level was taken using the modified Bergstrom needle technique with suction⁸⁰. A ~200 mg sample of muscle was obtained, rinsed in sterile phosphate-buffered saline solution (PBS) and portioned out for the various following analyses. The first half of the sample (~100 mg) was kept in sterile SK-MAX media (Wisent Bio) on ice for muscle stem cell isolation. The second half of the muscle sample was separated in two parts that were flash frozen for qPCR analysis (50 mg) or embedded in OCT tissue freezing medium and frozen in 2-methylbutane cooled in liquid nitrogen (50 mg). The samples were stored at -80 °C.

Myogenic cell lines isolation, purification, and culture

Muscle biopsies from controls and patients were minced, and plated in a culture dish⁸¹. Myoblasts were grown in Sk-MAX media complemented with Sk-MAX supplement and 20% fetal bovine serum (FBS). Myoblasts were expanded for a few days until there were enough cells for purification by FACS. Myoblasts were stained with 7-AAD (cell viability) and with the positive selection marker anti-CD56 AF647-conjugated (clone R19-760, 1:10, BD biosciences). Of note, preliminary experiments showed that virtually all CD56+ cells were also positive for another myogenic marker CD82⁸², and therefore only CD56 was used for the follow-up experiments. Myoblast differentiation was induced by exposing cells to 2% horse serum (HS) in DMEM media. Control and DMI myoblasts were used for experiments at the same low passage.

Conditioned media assay

For the proliferation assay, DMI myoblasts were treated with A1155463 (100 nM; Selleck Chemicals, S7800) or vehicle (DMSO) for 1 day in

proliferation media and the conditioned media (CM) was collected 4 days after the treatment and centrifuged at 800 x g for 5 minutes. The CM was used on healthy control myoblasts for 4-5 days and renewed every 2 days⁸³. Cells were incubated in the IncuCyte (Essen Bioscience), an automated microscope located in the cell culture incubator that automatically takes pictures and performs unbiased analysis of cell numbers. For the differentiation assay, control and DMI myoblasts were cultured in proliferation media until they reached 70% of confluence. Then, the media was changed to a differentiation media (DMEM low glucose, 2% horse serum) for 1 day and the condition media collected and centrifuged at 800 x g for 5 minutes. Then, the CM was incubated for 2 days on healthy control myotubes that have already been differentiated for 3 days. Fusion index was calculated based on the proportion of nuclei located in multinucleated myotubes (>2 nuclei) divided by total nuclei.

Single-cell RNA-sequencing experiments

Control and DMI myogenic cell lines were labeled with TotalSeq-B/Hashtag antibodies (Biolegend), following the manufacturer's recommendation. Each of the dissociated cell lines were stained with bar-coded TotalSeq-B antibodies targeting human CD298 and β 2 microglobulin (TotalSeq™-B0251 anti-human Hashtag 1 Antibody, cat. number 394631; TotalSeq™-B0252 anti-human Hashtag 2 Antibody, cat. number 394633; TotalSeq™-B0253 anti-human Hashtag 3 Antibody, cat. number 394635) for 30 min at 4 °C. Pooled single-cell suspensions were then resuspended in PBS containing 0.04% ultra-pure BSA. scRNAseq libraries were prepared using the Chromium Single Cell 30 Reagent Kits v3.1 (10x Genomics; Pleasanton, CA, USA) according to the manufacturer's instructions⁸⁴. Generated libraries were sequenced on an Illumina HiSeq4000.

Raw sequencing data were preprocessed using Cell Ranger 6.1.2⁸⁵ to perform the alignment (human genome GRCh38-2020-A), filtering, barcode counting, and UMI counting at a single-cell resolution, generating a control, patient, and a merged digital gene expression (DGE) matrix containing 1,902, 2,029 and 3,931 cells respectively. Further downstream analyses were conducted using R package Seurat v4.0 (spatial reconstruction of single-cell gene expression data⁸⁶) and singleCellTK v2.2.0 (Single cell Toolkit).

Quality control: Due to deep sequencing of the libraries, for each DGE matrix, cells expressing fewer than 1,000 genes and more than 10% of mitochondrial genes were filtered out, leaving a total of 3,381 cells in the merged matrix (1,639 cells from controls and 1,742 cells from patients). For all cells, genes were excluded if they were expressed in less than 3 cells. We normalized the DGE matrices by the total number of UMIs in each cell and scaled by 10⁶ to yield counts per million (CPM). We natural log transformed these matrices after the addition of a pseudocount of 1 to avoid undefined values.

The 2000 most variable genes were selected for each DGE matrix, based on their relative dispersion (variance/mean) regarding to the expected value across genes with similar average expression⁸⁷. Next, we performed a linear transformation ('scaling') to each matrix to minimize variations due to technical noise or possible batch effects.

We used DoubletFinder⁸⁸ (v.2.0.2) to identify putative doublets in each DGE matrix relying solely on gene expression data. DoubletFinder requires three input parameters for the doublet classification: the number of expected real doublets (nExp), the number of artificial doublets (pN) and the neighborhood size (pK). We calculated the nExp by multiplying the number of cells by the expected doublet ratio (1.6%) based on 10x genomics Chromium user guide. To identify pN and pK values, we performed the parameter optimization of DoubletFinder resulting in a pN of 0.30 for all matrices and a pK of 0.24, 0.01 and 0.005 for the control, patient, and merged matrices respectively. After the removal of putative doublets, we remain with 1,613 cells in the control, 1,714 cells in the patient, and 3,327 cells in the merged matrix for downstream analyses.

We estimated cell cycle activity by scoring the expression of a set of S phase-associated and G2/M phase-associated genes, as implemented in Seurat⁸⁶.

To enable unsupervised clustering, we performed a linear dimensionality reduction with principal component analysis (PCA) on each DGE matrix using the highly variable genes previously identified. Once embedded in this PCA space, we applied a K-nearest neighbor (KNN) graph-based clustering approach and refine the edge weights between any two cells based on the shared overlap in their local neighborhoods, identifying the $k = 10$ nearest neighbors for each cell. To cluster the cells, we apply a Louvain algorithm⁸⁹ to iteratively group cells together, with the goal of optimizing the standard modularity function. A resolution of 0.3 was used in the patient matrix to identify more defined cell populations. The t-Distributed Stochastic Neighbor Embedding (tSNE)⁹⁰ and the Uniform Manifold Approximation and Projection (UMAP) were used to visualize the clustering results; however, UMAP was chosen because it provides a better separation of the groups.

We computed differentially expressed genes (DEGs) between controls and patients using the Wilcoxon rank-sum test with the Benjamini-Hochberg procedure for FDR control⁹¹, identifying positive and negative markers for each group. DEGs with $|\log_{2}FC| > 1.0$ and adjusted p -values $< 10^{-6}$ were considered. In addition, we also computed the proportion and the probability distribution of cells expressing each gene in each group.

To identify DEGs among patient clusters and patient cells after the senescence annotation (method described below), we used the model-based analysis of single-cell transcriptomics method (MAST)⁹². DEGs with $|\log_{2}FC| > 0.25$, $FDR < 0.05$, percentage cluster expression > 0.5 , percentage expression in the control group < 0.4 , and adjusted p -values < 0.01 were considered. For the senescent and non-senescent populations, DEGs with an adjusted p -values < 0.01 and $\log_{2}FC > 1.5$ in one condition and $\log_{2}FC < 1.5$ in the other condition were plotted regardless the expression of the control.

Gene Ontology terms were analyzed for DEGs identified in each cell type using the online Metascape tool (<https://metascape.org>, v3.5)⁹³ with default parameters: Min Overlap = 3, p -value Cut-off = 0.05, and Min Enrichment = 1.5. The top 20 terms ranked by p -value were displayed in a bar diagram. Pathway enrichment analysis was performed using R package ReactomePA v1.36.0 and displayed in a bubble diagram⁹⁴.

To perform the annotation of senescent and non-senescent cells in patient cells, we used the R package GSVA v1.40.1⁹⁵ to compare the average expression of the DEGs of each patient cluster with reference gene sets related to cellular senescence and secretory processes^{38,96–98}. Heatmap and density plots are displayed. Clusters with GSVA scores > 0 in all gene sets were annotated as fully senescent cells, clusters with GSVA scores < 0 in all gene sets were annotated as non-senescent cells, and clusters with positive and negative GRVA values were annotated as early senescent cells.

Senescence-associated beta-galactosidase staining

CellEvent, senescence green detection kit (ThermoFisher, C10850) was used to label senescent cells according to the manufacturer's specifications. The fluorescent probe included in the assay is a substrate for beta-galactosidase and emits a 488 AlexaFluor fluorogenic signal in cells containing the beta-galactosidase active enzyme.

Fluorescence in situ hybridization (FISH)

Following the SA- β -gal staining protocol, cells were fixed with 2% PFA solution for 10 min at room temperature, washed, and dehydrated in prechilled 70% ethanol for 3 h at 4 °C. Thereafter, cells were washed in PBS RNase free for 10 min, incubated in 40% formamide (Millipore, Ca) in 2 \times saline-sodium citrate (SSC) buffer (300 mM sodium chloride, 30 mM sodium citrate, pH 7.0) for 10 min at room temperature, and

blocked in hybridization buffer (40% formamide, 2 \times SSC buffer, 200 μ g/mL bovine serum albumin, 100 mg/mL dextran sulfate, 2 mM vanadyl sulfate, 1 mg/mL yeast tRNA) for 15 min at 37 °C⁹⁹. The Cy5-labeled (CAG)₁₀ DNA probe was denatured for 10 min at 100 °C, chilled on ice for 10 min, then added to prechilled hybridization buffer for a final concentration of 150 ng/ μ L probe. Cells were incubated with the probe for 2 h at 37 °C. As a negative control, RNase solution were incubated for 10 min at RT before the hybridization of the probe. Cells were washed, counterstained with DAPI, and images were acquired on SP8 confocal microscope (Leica).

RT-qPCR

Myogenic cells' total RNA was extracted with Qiazol reagent according to the manufacturer's specifications. Total RNA was quantified with a Thermo Scientific™ NanoDrop™ 8000 Spectrophotometer. Reverse transcription was performed on 1 μ g of total RNA using the RT mastermix (QuantiTect Reverse Transcription Kit, 205313) to obtain cDNA. qPCR was performed with a set of primers designed on Primer-BLAST (NCBI) and validated for their specificity, efficiency and annealing temperature¹⁰⁰. Gene amplification was performed with the BlasTaq™ 2X qPCR MasterMix (Abm, G892) on a Roche LightCycler® 480 Instrument II. Data were analyzed with the LightCycler® 480 and were normalized relative to RPLPO expression¹⁰¹. The primers used are shown in Supplementary Table 4.

Immunofluorescence

Muscle biopsies were cut at 10 μ m thick in using a NX50 Cryostar (Thermo). Slices were put on positively charged Superfrost slides. Immunostaining was performed on skeletal muscle sections or on primary myoblast cultured on plastic dishes¹⁰². Samples were fixed with 2% PFA for 5 min (sections) or 10 min (cells). Sections were incubated with a blocking solution containing 5% of donkey serum and 2% of bovine serum albumin (BSA) in PBS for 60 minutes at room temperature. Sections were incubated overnight at 4 °C with the following primary antibodies diluted in blocking solution: PAX7 (clone PAX7, 1:20; Developmental Studies Hybridoma Bank, DSHB), P16 (ab54210, 1:50; Abcam), KI67 (14-5698-82, clone SolA15, 1:500; Invitrogen), Myosin Heavy Chain (MF-20, 1:10; DSHB), desmin (clone D33, 1:200; Agilent Dako), MYOG (ab124800, clone EPR4789, 1:200; Abcam), hDMD (MANDYS106(2c6), 1:2; DSHB), total DMD (ab15277, 1:200; Abcam). Secondary antibodies were also diluted in blocking buffer (1:1,000) and incubated for 1 h at room temperature. Secondary antibodies (Invitrogen) used were donkey anti-mouse 488 (A21202) or donkey anti-mouse 594 (A21203), donkey anti-rabbit 488 (A21206) or donkey anti-rabbit 647 (A32795). Slides were mounted using PermaFluor mounting medium (Fisher Scientific). Immunofluorescence pictures of samples were taken with EVOS M5000 (Thermo Fisher Scientific, EVOS M5000 Software Revision 1.5.1500.493) or Leica TCS SP8 DLS confocal microscope. Pictures were analyzed using ImageJ software (version 1.53, National Institutes of Health, USA).

Oxidative stress detection

CellROX Deep red reagent (ThermoFisher, C10422) was combined with CellEvent, senescence green detection kit (ThermoFisher, C10840) for measuring cellular oxidative stress in senescent cells according to manufacturer's specifications. The CellROX was added to the myoblasts at a final concentration of 5 μ M for 30 minutes at 37 °C in the cell culture incubator. Cells were washed, trypsinized and fixed with PFA 3.7% for 15 minutes. Afterward, CellEvent staining was performed for 1 h at 37 °C in an incubator without CO₂. The signal was detected with a Flow cytometer (BD FACSCantoII) and analyzed with FlowJo.

Viability assay

Cell viability was determined by Cell-titer 96 aqueous one solution cell proliferation assay kit (Promega, G3580) according to the

manufacturer's specifications. Briefly, aliquots of 5×10^3 cells/well were cultured in 96-well plates. After 24 hours in culture, cells were treated with vehicle (DMSO) or the following senolytics: FOXO4-DRI (NovoPro), Fisetin (Selleck chemicals), Dasatinib + Quercetin (Sigma), Navitoclax (ABT-263, Abcam), A1331852 (Selleck Chemicals), or A1155463 (Selleck Chemicals), at different concentrations for 48 h. Then, 40 μ l of Cell-titer 96 aqueous one solution was added to each well and incubated for an additional 3 h. The absorbance at 490 nm was recorded with a 96-well plate reader (BMG Labtech, CLARIOstar).

Apoptosis assay

Apoptotic cells were identified using a detection kit (Biolegend, FITC Annexin V Apoptosis Detection Kit with PI, 640914) according to manufacturer's specifications. After trypsinization, cells were washed twice with Cell Staining Buffer and stained with FITC Annexin V (1:30) and PI (1:10) for 15 minutes at room temperature. Then, 400 μ l of Annexin V binding buffer was added, and the samples were analyzed by LSR Fortessa cytometer (BD Biosciences).

SASP markers Luminex assay

A multiplex Luminex assay (Eve Technologies, Calgary, Alberta) was used to measure SASP markers of myogenic cells supernatant media. Two different discovery assays were chosen to assess SASP markers: Human Cytokine/Chemokine 48-Plex Discovery Assay[®] Array (HD48) and Human MMP and TIMP Discovery Assay[®] Array. Cells were treated with senolytic or vehicle and incubated for 36 hours. Cell media was changed, and cells were incubated for another 36 hours before supernatant collection. Supernatants were stored at -80°C until assayed.

Western blot

Cells were washed with sterile PBS and lysed with ice-cold RIPA buffer containing 1% of protease inhibitors and centrifuged at 10,000 g for 10 min. The supernatant was retained, aliquoted, and the protein content was quantified using the BCA Assay Kit (Thermo scientific, Mississauga, Ontario, Canada). A volume corresponding to 40 μ g of protein was diluted with a sample buffer (125 mM Tris buffer (pH 6.8), 4% SDS, 20% glycerol, 0.05% bromophenol blue, and 200 mM dithiothreitol), heated at 100°C for 5 min and electroseparated on 10% sodium dodecyl sulfate-polyacrylamide gel¹⁰³. Proteins were transferred to polyvinylidene difluoride membranes, which were blocked with 5% non-fat milk or 5% BSA for 90 min at room temperature. Membranes were immunoblotted overnight at 4°C with anti-myogenin (ab124800, 1:500; Abcam) and anti-beta-actin (4967 S, 1:5,000; Cell Signaling) as primary antibodies. After washing, membranes were incubated with goat anti-rabbit (H + L) HRP-conjugated secondary antibody (1:5,000; Abcam, ab6721) for 1 h at room temperature. Bands were revealed with ECL-plus Western blotting reagent (PerkinElmer Life and Analytical Sciences, USA), visualized using G:Box (GeneSys imaging software, v1.8.6.0), and quantified using ImageJ (v1.53, National Institutes of Health, Maryland, USA). Densities were normalized to the loading control.

Cell transplantation assay

Eight weeks old NOD/SCID/IL2R γ null (NSG) male mice (Jackson Laboratory: 005557) were housed in the animal care facility at the CHU Sainte-Justine Research Center under pathogen-free conditions in sterile ventilated racks. Mice were housed on a 12:12 h light:dark cycle at 21°C and 40% humidity, and they had free access to food (Harlan Teklad 2918) and tap water. All animal experiments were previously approved by the institutional committee for good laboratory practices for animal research of the CHU Sainte-Justine research center (CIBPAR protocol #2020-2357) in accordance with the Canadian Council on Animal Care guidelines. To induce muscle regeneration and enhance cellular engraftment, a cardiotoxin injection (Latoxan, 50 μ l of 10 μ M

solution in saline) was performed intramuscularly (i.m.) through the skin in the right and left tibialis anterior (TA) muscles under general anesthesia. After 24 hours, 2×10^5 DMI myoblasts (resuspended in 10 ml of PBS) that were previously treated with A1155463 or vehicle for 72 hours were transplanted into the right or left injured TA muscle, respectively¹⁰⁴. Three different cell lines were used, and each cell line was transplanted into 3 different mice. Mice were allowed to recover for 20 days after which they were euthanized by CO_2 inhalation (under anesthesia) followed by cervical dislocation and their TA muscles were collected. Tissues were embedded in OCT tissue freezing medium and frozen in 2-methylbutane cooled in liquid nitrogen and stored at -80°C until sectioning. Muscle sections from 3 different regions (proximal, median and distal) of the TA muscle were collected. Out of each region, we cut at least 3 sections and acquired the images for the quantification analysis. Only myofibers presenting double positive for hDMD and DMD were considered as successfully transplanted.

Statistical analysis

Sample size determination was based on the expected effect size and variability that was previously published for similar readouts using DMI patient myogenic cultures^{5,12}. No data were excluded, except in rare cases of major experimental issues (e.g., animal's death). All experiments were repeated independently at least twice in the laboratory with similar results. For each set of experiments, the proportion of control and DMI patients were matched as best as possible for age and sex. For data collection and analysis, the experimenter was blinded to the identity of the sample. For in vitro experiments, data were analyzed using GraphPad Prism (version 9.1.0). Normality was verified for all data according to the Shapiro–Wilk test. Treatment effects were determined using unpaired t-test, One-Way ANOVA with Sidak's multiple comparisons test, or 2-way ANOVA followed by Bonferroni's multiple comparisons depending on the experimental setup. Results are reported as mean \pm standard error of the mean (SEM). For in vivo data analyses, associations between IL-6 level and muscle strength and functional capacity of patients were assessed using Spearman ρ correlation coefficient. Comparisons of muscle strength and functional capacity between patients based on IL-6 normative value for healthy individuals (below or over the threshold) were performed using Mann-Whitney U Test. Stepwise multiple regression analyses were used to determine which variables among age, sex, phenotype and IL-6 level (low or high) best explain each variable of muscle strength and functional capacity. For all tests, the significance value was set at p -value $< .05$. In vivo data were analyzed using IBM SPSS Statistics for Windows, Version 24.0 (Armonk, NY: IBM Corp).

Reporting summary

Further information on research design is available in the Nature Portfolio Reporting Summary linked to this article.

Data availability

The raw data generated for the main figures are provided in the Source data file. Single-cell RNA seq data have been deposited to Gene Expression Omnibus under accession number GSE208360. The analysis on the SASP Atlas (Supplementary Fig. 3) was based on the datasets MassIVE ID number: MSV000083750 and ProteomeXchange ID number: PXD013721 (or can be visualized on www.saspatlas.com). The analysis of *DMPK* expression during muscle regeneration (Supplementary Fig. 6) was based on the dataset GSE138826. Source data are provided in this paper.

References

1. Bouchard, G., Roy, R., Declos, M., Mathieu, J. & Kouladjian, K. Origin and diffusion of the myotonic dystrophy gene in the Saguenay region (Quebec). *Can J Neurol Sci* **16**, 119–122 (1989).

2. Liao, Q., Zhang, Y., He, J. & Huang, K. Global prevalence of myotonic dystrophy: an updated systematic review and meta-analysis. *Neuroepidemiology* **56**, 163–173 (2022).
3. Fu, Y. H. et al. An unstable triplet repeat in a gene related to myotonic muscular dystrophy. *Science* **255**, 1256–1258 (1992).
4. Savic, D. et al. 250 CTG repeats in DMPK is a threshold for correlation of expansion size and age at onset of juvenile-adult DM1. *Hum. Mutat.* **19**, 131–139 (2002).
5. Thornell, L. E. et al. Satellite cell dysfunction contributes to the progressive muscle atrophy in myotonic dystrophy type 1. *Neuropathol. Appl. Neurobiol.* **35**, 603–613 (2009).
6. Hunter, A. et al. The correlation of age of onset with CTG trinucleotide repeat amplification in myotonic dystrophy. *J. Med. Genet.* **29**, 774–779 (1992).
7. Tsilfidis, C., MacKenzie, A. E., Mettler, G., Barcelo, J. & Korneluk, R. G. Correlation between CTG trinucleotide repeat length and frequency of severe congenital myotonic dystrophy. *Nat. Genet.* **1**, 192–195 (1992).
8. De Antonio, M. et al. Unravelling the myotonic dystrophy type 1 clinical spectrum: A systematic registry-based study with implications for disease classification. *Rev. Neurol.* **172**, 572–580 (2016).
9. Gagnon, C. et al. A 9-year follow-up study of quantitative muscle strength changes in myotonic dystrophy type 1. *J. Neurol.* **265**, 1698–1705 (2018).
10. Dumont, N. A., Bentzinger, C. F., Sincennes, M. C. & Rudnicki, M. A. Satellite cells and skeletal muscle regeneration. *Compr. Physiol.* **5**, 1027–1059 (2015).
11. Meinke, P., Hintze, S., Limmer, S. & Schoser, B. Myotonic dystrophy-A progeroid disease? *Front. Neurol.* **9**, 601 (2018).
12. Bigot, A. et al. Large CTG repeats trigger p16-dependent premature senescence in myotonic dystrophy type 1 muscle precursor cells. *Am. J. Pathol.* **174**, 1435–1442 (2009).
13. Renna, L. V. et al. Premature senescence in primary muscle cultures of myotonic dystrophy type 2 is not associated with p16 induction. *Eur. J. Histochem.* **58**, 2444 (2014).
14. Hasuike, Y., Mochizuki, H. & Nakamori, M. Expanded CUG repeat RNA induces premature senescence in myotonic dystrophy model cells. *Front. Genet.* **13**, 865811 (2022).
15. Munoz-Espin, D. & Serrano, M. Cellular senescence: from physiology to pathology. *Nat. Rev. Mol. Cell Biol.* **15**, 482–496 (2014).
16. Coppe, J. P. et al. Senescence-associated secretory phenotypes reveal cell-nonautonomous functions of oncogenic RAS and the p53 tumor suppressor. *PLoS Biol.* **6**, 2853–2868 (2008).
17. Haddad, F., Zaldivar, F., Cooper, D. M. & Adams, G. R. IL-6-induced skeletal muscle atrophy. *J. Appl. Physiol.* (1985) **98**, 911–917 (2005).
18. Bian, A. L. et al. A study on relationship between elderly sarcopenia and inflammatory factors IL-6 and TNF-alpha. *Eur. J. Med. Res.* **22**, 25 (2017).
19. Tierney, M. T. et al. STAT3 signaling controls satellite cell expansion and skeletal muscle repair. *Nat. Med.* **20**, 1182–1186 (2014).
20. Baker, D. J. et al. Naturally occurring p16(Ink4a)-positive cells shorten healthy lifespan. *Nature* **530**, 184–189 (2016).
21. de Keizer, P. L. The fountain of youth by targeting senescent cells. *Trends Mol. Med.* **23**, 6–17 (2017).
22. Baker, D. J. et al. Clearance of p16Ink4a-positive senescent cells delays ageing-associated disorders. *Nature* **479**, 232–236 (2011).
23. van Deursen, J. M. Senolytic therapies for healthy longevity. *Science* **364**, 636–637 (2019).
24. Xu, M. et al. Senolytics improve physical function and increase lifespan in old age. *Nat. Med.* **24**, 1246–1256 (2018).
25. Gallais, B., Gagnon, C., Mathieu, J. & Richer, L. Cognitive decline over time in adults with myotonic dystrophy type 1: A 9-year longitudinal study. *Neuromuscul. Disord.* **27**, 61–72 (2017).
26. Mateos-Aierdi, A. J. et al. Muscle wasting in myotonic dystrophies: a model of premature aging. *Front. Aging Neurosci.* **7**, 125 (2015).
27. De Buck, M. et al. The cytokine-serum amyloid A-chemokine network. *Cytokine Growth Factor Rev.* **30**, 55–69 (2016).
28. Binet, F. et al. Neutrophil extracellular traps target senescent vasculature for tissue remodeling in retinopathy. *Science* **369**, eaay5356 (2020).
29. Freund, A., Orjalo, A. V., Desprez, P. Y. & Campisi, J. Inflammatory networks during cellular senescence: causes and consequences. *Trends Mol. Med.* **16**, 238–246 (2010).
30. Basisty, N. et al. A proteomic atlas of senescence-associated secretomes for aging biomarker development. *PLoS Biol.* **18**, e3000599 (2020).
31. Hogrel, J. Y. et al. Development of a French isometric strength normative database for adults using quantitative muscle testing. *Arch. Phys. Med. Rehabil.* **88**, 1289–1297 (2007).
32. Todd, J., Simpson, P., Estis, J., Torres, V. & Wub, A. H. Reference range and short- and long-term biological variation of interleukin (IL)-6, IL-17A and tissue necrosis factor-alpha using high sensitivity assays. *Cytokine* **64**, 660–665 (2013).
33. Roussel, M. P., Hebert, L. J. & Duchesne, E. Intra-rater reliability and concurrent validity of quantified muscle testing for maximal knee extensors strength in men with myotonic dystrophy type 1. *J. Neuromuscul. Dis.* **6**, 233–240 (2019).
34. Knak, K. L., Sheikh, A. M., Andersen, H., Witting, N. & Vissing, J. Intrarater reliability and validity of outcome measures in myotonic dystrophy type 1. *Neurology* **94**, e2508–e2520 (2020).
35. Zhu, Y. et al. New agents that target senescent cells: the flavone, fisetin, and the BCL-XL inhibitors, A1331852 and A1155463. *Aging* **9**, 955–963 (2017).
36. Zhu, M., Meng, P., Ling, X. & Zhou, L. Advancements in therapeutic drugs targeting of senescence. *Ther. Adv. Chronic Dis.* **11**, 2040622320964125 (2020).
37. Baar, M. P. et al. Targeted apoptosis of senescent cells restores tissue homeostasis in response to chemotoxicity and aging. *Cell* **169**, 132–147.e116 (2017).
38. Chang, J. et al. Clearance of senescent cells by ABT263 rejuvenates aged hematopoietic stem cells in mice. *Nat. Med.* **22**, 78–83 (2016).
39. Saito, Y. & Chikenji, T. S. Diverse roles of cellular senescence in skeletal muscle inflammation, regeneration, and therapeutics. *Front. Pharmacol.* **12**, 739510 (2021).
40. Garcia-Puga, M. et al. Senescence plays a role in myotonic dystrophy type 1. *JCI Insight* **7**, e159357 (2022).
41. DMPK. The Human Protein Atlas. <https://www.proteinatlas.org/ENSG00000104936-DMPK/single+cell+type/skeletal+muscle>.
42. Karlsson, M. et al. A single-cell type transcriptomics map of human tissues. *Sci. Adv.* **7**, eabh2169 (2021).
43. Nakamori, M. et al. Aberrant myokine signaling in congenital myotonic dystrophy. *Cell Rep.* **21**, 1240–1252 (2017).
44. Usuki, F. & Ishiura, S. Expanded CTG repeats in myotonin protein kinase increase susceptibility to oxidative stress. *Neuroreport* **9**, 2291–2296 (1998).
45. Toscano, A. et al. Oxidative stress in myotonic dystrophy type 1. *Free Radic. Res.* **39**, 771–776 (2005).
46. Ihara, Y. et al. Free radicals, lipid peroxides and antioxidants in blood of patients with myotonic dystrophy. *J. Neurol.* **242**, 119–122 (1995).
47. La Rosa, P., Petrillo, S., Bertini, E. S. & Piemonte, F. Oxidative stress in DNA repeat expansion disorders: a focus on NRF2 signaling involvement. *Biomolecules* **10**, 702 (2020).
48. Roma-Mateo, C. et al. Oxidative stress and the epigenetics of cell senescence: insights from progeroid syndromes. *Curr. Pharm. Des.* **24**, 4755–4770 (2018).

49. Yang, S. R., Park, J. R. & Kang, K. S. Reactive oxygen species in mesenchymal stem cell aging: implication to lung diseases. *Oxid. Med. Cell Longev.* **2015**, 486263 (2015).
50. Todorow, V. et al. Transcriptome analysis in a primary human muscle cell differentiation model for myotonic dystrophy type 1. *Int. J. Mol. Sci.* **22**, 8607 (2021).
51. Wang, E. T. et al. Transcriptome alterations in myotonic dystrophy skeletal muscle and heart. *Hum. Mol. Genet.* **28**, 1312–1321 (2019).
52. Espinosa-Espinosa, J., Gonzalez-Barriga, A., Lopez-Castel, A. & Artero, R. Deciphering the complex molecular pathogenesis of myotonic dystrophy type 1 through omics studies. *Int. J. Mol. Sci.* **23**, 1441 (2022).
53. Franck, S. et al. Myotonic dystrophy type 1 embryonic stem cells show decreased myogenic potential, increased CpG methylation at the DMPK locus and RNA mis-splicing. *Biol. Open* **11**, bio058978 (2022).
54. Andre, L. M. et al. Recovery in the myogenic program of congenital myotonic dystrophy myoblasts after excision of the expanded (CTG)_n repeat. *Int. J. Mol. Sci.* **20**, 5685 (2019).
55. Rivera-Mulia, J. C. et al. DNA replication timing alterations identify common markers between distinct progeroid diseases. *Proc. Natl Acad. Sci. USA* **114**, E10972–E10980 (2017).
56. Davey, E. E. et al. Individual transcriptomic response to strength training for myotonic dystrophy type 1 patients *JCI Insight* <https://doi.org/10.1172/jci.insight.163856>, e163856 (2023).
57. Otero, B. A. et al. Transcriptome alterations in myotonic dystrophy frontal cortex. *Cell Rep.* **34**, 108634 (2021).
58. Hari, P. et al. The innate immune sensor Toll-like receptor 2 controls the senescence-associated secretory phenotype. *Sci. Adv.* **5**, eaaw0254 (2019).
59. Admasu, T. D., Rae, M. & Stolzing, A. Dissecting primary and secondary senescence to enable new senotherapeutic strategies. *Ageing Res. Rev.* **70**, 101412 (2021).
60. da Silva, P. F. L. et al. The bystander effect contributes to the accumulation of senescent cells in vivo. *Ageing Cell* **18**, e12848 (2019).
61. Kirkland, J. L. & Tchkonina, T. Senolytic drugs: from discovery to translation. *J. Intern. Med.* **288**, 518–536 (2020).
62. Ge, M. et al. Senolytic targets and new strategies for clearing senescent cells. *Mech. Ageing Dev.* **195**, 111468 (2021).
63. Sevilla, L., Zaldumbide, A., Pognonec, P. & Boulukos, K. E. Transcriptional regulation of the bcl-x gene encoding the anti-apoptotic Bcl-xL protein by Ets, Rel/NFκB, STAT and AP1 transcription factor families. *Histol. Histopathol.* **16**, 595–601 (2001).
64. Wilson, E. M., Tureckova, J. & Rotwein, P. Permissive roles of phosphatidylinositol 3-kinase and Akt in skeletal myocyte maturation. *Mol. Biol. Cell* **15**, 497–505 (2004).
65. Contreras, O., Villarreal, M. & Brandan, E. Nilotinib impairs skeletal myogenesis by increasing myoblast proliferation. *Skelet. Muscle* **8**, 5 (2018).
66. Liu, M. et al. Phosphorylated GSK-3β protects stress-induced apoptosis of myoblasts via the PI3K/Akt signaling pathway. *Mol. Med. Rep.* **22**, 317–327 (2020).
67. Gros, M. et al. Identification of serum interleukin 6 levels as a disease severity biomarker in facioscapulohumeral muscular dystrophy. *J. Neuromuscul. Dis.* **9**, 83–93 (2022).
68. Overend, G. et al. Allele length of the DMPK CTG repeat is a predictor of progressive myotonic dystrophy type 1 phenotypes. *Hum. Mol. Genet.* **28**, 2245–2254 (2019).
69. Sugihara, H., Teramoto, N., Yamanouchi, K., Matsuwaki, T. & Nishihara, M. Oxidative stress-mediated senescence in mesenchymal progenitor cells causes the loss of their fibro/adipogenic potential and abrogates myoblast fusion. *Ageing* **10**, 747–763 (2018).
70. Gomes-Pereira, M., Cooper, T. A. & Gourdon, G. Myotonic dystrophy mouse models: towards rational therapy development. *Trends Mol. Med.* **17**, 506–517 (2011).
71. Mahadevan, M. S. et al. Reversible model of RNA toxicity and cardiac conduction defects in myotonic dystrophy. *Nat. Genet.* **38**, 1066–1070 (2006).
72. Huguet, A. et al. Molecular, physiological, and motor performance defects in DMSXL mice carrying >1000 CTG repeats from the human DM1 locus. *PLoS Genet.* **8**, e1003043 (2012).
73. Rao, A. N. et al. Reversible cardiac disease features in an inducible CUG repeat RNA-expressing mouse model of myotonic dystrophy. *JCI Insight* **6**, e143465 (2021).
74. Yadava, R. S. et al. Modeling muscle regeneration in RNA toxicity mice. *Hum. Mol. Genet.* **30**, 1111–1130 (2021).
75. Mankodi, A. et al. Myotonic dystrophy in transgenic mice expressing an expanded CUG repeat. *Science* **289**, 1769–1773 (2000).
76. Pascual-Gilabert, M., Lopez-Castel, A. & Artero, R. Myotonic dystrophy type 1 drug development: a pipeline toward the market. *Drug Discov. Today* **26**, 1765–1772 (2021).
77. Petitclerc, E., Hebert, L. J., Mathieu, J., Desrosiers, J. & Gagnon, C. Lower limb muscle strength impairment in late-onset and adult myotonic dystrophy type 1 phenotypes. *Muscle Nerve* **56**, 57–63 (2017).
78. Raymond, K. et al. Predictors of participation restriction over a 9-year period in adults with myotonic dystrophy type 1. *Disabil. Rehabil.* **44**, 2615–2631 (2020).
79. Jimenez-Moreno, A. C. et al. Analysis of the functional capacity outcome measures for myotonic dystrophy. *Ann. Clin. Transl. Neurol.* **6**, 1487–1497 (2019).
80. Shanely, R. A. et al. Human skeletal muscle biopsy procedures using the modified Bergstrom technique. *J. Vis. Exp.* **91**, 51812 (2014).
81. Sasarman, F., Karpati, G. & Shoubbridge, E. A. Nuclear genetic control of mitochondrial translation in skeletal muscle revealed in patients with mitochondrial myopathy. *Hum. Mol. Genet.* **11**, 1669–1681 (2002).
82. Alexander, M. S. et al. CD82 is a marker for prospective isolation of human muscle satellite cells and is linked to muscular dystrophies. *Cell Stem Cell* **19**, 800–807 (2016).
83. Dort, J. et al. Resolvin-D2 targets myogenic cells and improves muscle regeneration in Duchenne muscular dystrophy. *Nat. Commun.* **12**, 6264 (2021).
84. Zarkada, G. et al. Specialized endothelial tip cells guide neuroretina vascularization and blood-retina-barrier formation. *Dev. Cell* **56**, 2237–2251.e2236 (2021).
85. Zheng, G. X. et al. Massively parallel digital transcriptional profiling of single cells. *Nat. Commun.* **8**, 14049 (2017).
86. Hao, Y. et al. Integrated analysis of multimodal single-cell data. *Cell* **184**, 3573–3587.e3529 (2021).
87. Brennecke, P. et al. Accounting for technical noise in single-cell RNA-seq experiments. *Nat. Methods* **10**, 1093–1095 (2013).
88. McGinnis, C. S., Murrow, L. M. & Gartner, Z. J. DoubletFinder: doublet detection in single-cell RNA sequencing data using artificial nearest neighbors. *Cell Syst.* **8**, 329–337.e324 (2019).
89. Blondel, V. D., Guillaume, J.-L., Lambiotte, R. & Lefebvre, E. Fast unfolding of communities in large networks. *J. Stat. Mech. Theory Exp.* **2008**, P10008 (2008).
90. van der Maaten, L. & Hinton, G. Visualizing data using t-SNE. *J. Mach. Learn. Res.* **9**, 2579–2605 (2008).
91. Benjamini, Y. & Hochberg, Y. Controlling the False Discovery Rate: A Practical and Powerful Approach to Multiple Testing. *J. R. Stat. Soc.: Ser. B (Methodol.)* **57**, 289–300 (1995).
92. Finak, G. et al. MAST: a flexible statistical framework for assessing transcriptional changes and characterizing heterogeneity in single-cell RNA sequencing data. *Genome Biol.* **16**, 278 (2015).

93. Zhou, Y. et al. Metascape provides a biologist-oriented resource for the analysis of systems-level datasets. *Nat. Commun.* **10**, 1523 (2019).
94. Yu, G. & He, Q. Y. ReactomePA: an R/Bioconductor package for reactome pathway analysis and visualization. *Mol. Biosyst.* **12**, 477–479 (2016).
95. Hanzelmann, S., Castelo, R. & Guinney, J. GSEA: gene set variation analysis for microarray and RNA-seq data. *BMC Bioinform.* **14**, 7 (2013).
96. Ashburner, M. et al. Gene ontology: tool for the unification of biology. The Gene Ontology Consortium. *Nat. Genet.* **25**, 25–29 (2000).
97. Gene Ontology, C. The Gene Ontology resource: enriching a Gold mine. *Nucleic Acids Res.* **49**, D325–D334 (2021).
98. Fridman, A. L. & Tainsky, M. A. Critical pathways in cellular senescence and immortalization revealed by gene expression profiling. *Oncogene* **27**, 5975–5987 (2008).
99. Xia, G. et al. Generation of neural cells from DM1 induced pluripotent stem cells as cellular model for the study of central nervous system neuropathogenesis. *Cell Reprogram.* **15**, 166–177 (2013).
100. Bhatnagar, S., Panguluri, S. K. & Kumar, A. Gene profiling studies in skeletal muscle by quantitative real-time polymerase chain reaction assay. *Methods Mol. Biol.* **798**, 311–324 (2012).
101. Stern-Straeter, J., Bonaterra, G. A., Hormann, K., Kinscherf, R. & Goessler, U. R. Identification of valid reference genes during the differentiation of human myoblasts. *BMC Mol. Biol.* **10**, 66 (2009).
102. Dumont, N. A. & Rudnicki, M. A. Characterizing satellite cells and myogenic progenitors during skeletal muscle regeneration. *Methods Mol. Biol.* **1560**, 179–188 (2017).
103. Deprez, A. et al. Transient neonatal exposure to hyperoxia, an experimental model of preterm birth, leads to skeletal muscle atrophy and fiber type switching. *Clin. Sci.* **135**, 2589–2605 (2021).
104. Fabre, P., Molina, T., Orfi, Z. & Dumont, N. A. Assessment of Muscle Function Following hiPSC-Derived Myoblast Transplantation in Dystrophic Mice. *Curr. Protoc.* **2**, e356 (2022).
- S.M. (#284100) were supported by FRQS Junior-2 award, and C.G. (#31011) was supported by FRQS Senior award. This study was supported by grants from Canadian Institutes of Health Research (CIHR) (grant no. MOP-49556 (C.G.), JNM-108412 (C.G.), PJT-186092 (N.A.D. and E.D.), the Quebec Cell, Tissue and Gene Therapy Network –ThéCell (a thematic network supported by the FRQS; N.A.D. and E.D.) and Muscular Dystrophy Canada (#855145, N.A.D. and E.D.).

Acknowledgements

We thank M. Hicham Affia and Ms. Veronique Lisi for their technical assistance. We thank Sonja Lespérance for careful animal husbandry. T.C.C. was supported by a fellowship from the Myotonic Dystrophy Foundation. G.D.B. was supported by CHU Sainte-Justine, University of Montreal, and RQR (réseau québécois en reproduction) awards. Z.O. was supported by an award from the MITACS fellowship. I.M. was supported by CERMO-FC (Center of Excellence in Research on Orphan Diseases – Fondation Courtois) and TheCell awards. A.D. was supported by an FQRNT (Fonds Québécois de la recherche - nature et les technologies) doctoral award. M.P.R. and T.M. were supported by FRQS (Fonds Québécois de la recherche – Santé) doctoral awards. G.A. holds the Banque Nationale Research Excellence Chair in Cardiovascular Genetics. E.D. (#311186) was supported by FRQS Junior-1 award, N.A.D. (#296512) and

S.M. (#284100) were supported by FRQS Junior-2 award, and C.G. (#31011) was supported by FRQS Senior award. This study was supported by grants from Canadian Institutes of Health Research (CIHR) (grant no. MOP-49556 (C.G.), JNM-108412 (C.G.), PJT-186092 (N.A.D. and E.D.), the Quebec Cell, Tissue and Gene Therapy Network –ThéCell (a thematic network supported by the FRQS; N.A.D. and E.D.) and Muscular Dystrophy Canada (#855145, N.A.D. and E.D.).

Author contributions

N.A.D. and E.D. conceived and managed the project. T.C.C., G.D.B., Z.O., I.M., M.P.R., A.D., O.P., D.M., I.C., B.B., L.T., S.L., J.M., C.G., T.K., and T.M. designed and performed experiments, and collected data. J.M., C.G., G.A., C.B., S.M., T.C.C., L.F., G.D.B., I.C., E.D., and N.A.D. analyzed and interpreted the data. T.C.C., G.D.B., E.D., and N.A.D. wrote the manuscript. All authors carefully reviewed and provided critical insights into the manuscript.

Competing interests

The authors declare no competing interests.

Additional information

Supplementary information The online version contains supplementary material available at <https://doi.org/10.1038/s41467-023-39663-3>.

Correspondence and requests for materials should be addressed to Elise Duchesne or Nicolas A. Dumont.

Peer review information *Nature Communications* thanks the anonymous, reviewer(s) for their contribution to the peer review of this work.

Reprints and permissions information is available at <http://www.nature.com/reprints>

Publisher's note Springer Nature remains neutral with regard to jurisdictional claims in published maps and institutional affiliations.

Open Access This article is licensed under a Creative Commons Attribution 4.0 International License, which permits use, sharing, adaptation, distribution and reproduction in any medium or format, as long as you give appropriate credit to the original author(s) and the source, provide a link to the Creative Commons license, and indicate if changes were made. The images or other third party material in this article are included in the article's Creative Commons license, unless indicated otherwise in a credit line to the material. If material is not included in the article's Creative Commons license and your intended use is not permitted by statutory regulation or exceeds the permitted use, you will need to obtain permission directly from the copyright holder. To view a copy of this license, visit <http://creativecommons.org/licenses/by/4.0/>.

© The Author(s) 2023